

Near Surface Stratigraphy and Regolith Production in Southwestern Elysium Planitia, Mars: Implications for Hesperian-Amazonian Terrains and the InSight Lander Mission

N.H. Warner¹ · M.P. Golombek² · J. Sweeney¹ · R. Fergason³ · R. Kirk³ · C. Schwartz²

Received: 17 August 2016 / Accepted: 15 March 2017 / Published online: 10 April 2017
© Springer Science+Business Media Dordrecht 2017

Abstract The presence of rocks in the ejecta of craters at the InSight landing site in southwestern Elysium Planitia indicates a strong, rock-producing unit at depth. A finer regolith above is inferred by the lack of rocks in the ejecta of 10-m-scale craters. This regolith should be penetrable by the mole of the Heat Flow and Physical Properties Package (HP³). An analysis of the size-frequency distribution (SFD) of 7988 rocky ejecta craters (RECs) across four candidate landing ellipses reveals that all craters >200 m in diameter and <750 ± 30 Ma in age have boulder-sized rocks in their ejecta. The frequency of RECs however decreases significantly below this diameter (D), represented by a roll-off in the SFD slope. At 30 m < D < 200 m, the slope of the cumulative SFD declines to near zero at D < 30 m. Surface modification, resolution limits, or human counting error cannot account for the magnitude of this roll-off. Rather, a significant population of <200 m diameter fresh non-rocky ejecta craters (NRECs) here indicates the presence of a relatively fine-grained regolith that prevents smaller craters from excavating the strong rock-producing unit. Depth to excavation relationships and the REC size thresholds indicate the region is capped by a regolith that is almost everywhere 3 m thick but may be as thick as 12 to 18 m. The lower bound of the thickness range is independently confirmed by the depth to the inner crater in concentric or nested craters. The data indicate that 85% of the InSight landing region is covered by a regolith that is at least 3 m thick. The probability of encountering rockier material at depths >3 m by the HP³ however increases significantly due to the increase in boulder-size rocks in the lower regolith column, near the interface of the bedrock.

Keywords InSight · Regolith · Mars · Elysium Planitia · Hesperian · Amazonian · Craters · Ejecta · Crater counts · Heat Flow and Physical Properties Package · Erosion rates

✉ N.H. Warner
warner@geneseo.edu

¹ Department of Geological Sciences, State University of New York at Geneseo, 1 College Circle, Geneseo, NY, USA

² Jet Propulsion Laboratory, California Institute of Technology, Pasadena, CA, USA

³ Astrogeology Science Center, U.S. Geological Survey, Flagstaff, AZ, USA

1 Introduction

Regolith production by impact gardening is one of the most fundamental geologic processes that operates to modify planetary surfaces that lack thick atmospheres (e.g. Shoemaker et al. 1969; Hartmann 1973; Oberbeck and Quaide 1967; Hartmann et al. 2001; Wilcox et al. 2005; Bart et al. 2011). The thickness of this surficial layer is directly related to exposure age, impact production rate, crater size frequency distribution, and geologic processes that have an additive (e.g. sedimentary deposition) or subtractive (e.g. eolian erosion) effect on regolith production and stability. On the Moon, where regolith thickness and production rates are well studied (e.g. Oberbeck and Quaide 1968; Shoemaker et al. 1968; McKay et al. 1974, 1991; Shkuratov and Bondarenko 2001; Hartmann et al. 2001; Bart et al. 2011; Fa and Wicczorek 2012; Bart 2014), impact gardening, space weathering (e.g. solar and cosmic rays), and topography are the primary factors that influence the formation and stability of regolith. However, on Mars, the production of regolith is different from the Moon and is complicated by additional surface processes (e.g. wind). For example, while impact gardening is likely a major process by which regolith is produced on Mars (Hartmann 1973; Hartmann et al. 2001), lunar-style micrometeorite bombardment has been prevented by the (order of) 10 mbar-thick atmosphere. Rather, a fine-grained component of the martian regolith (Christensen and Moore 1992), including dust-sized up to sand sized particles, was produced through physical (e.g. Bridges et al. 2011) and chemical weathering of crustal rocks (e.g. Bishop et al. 2002; Banfield et al. 2003; Ruff 2004). The time-averaged rates of these processes and their role in producing regolith locally are dependent on when the surface was formed, the duration over which it was exposed, and its geologic and geomorphic characteristics. Air fall dust accumulation for instance may have contributed significantly to the formation of a fine-grained regolith component in some regions, while having little to no influence in other areas. Global and regional dust surveys (Moore and Edgett 1993; Banfield 2002; Mangold et al. 2009) and rover-based observations (Golombek et al. 1999, 2014a; Johnson et al. 2003; Ruff et al. 2006; Berger et al. 2016) indicate that the thickness of the global dust layer is non-uniform, ranging from zero (e.g. Meridiani Planum) to several tens of meters thick (e.g. Tharsis, Arabia Terra, Christensen and Moore 1992; Mangold et al. 2009). Global circulation patterns, regional/local wind regimes, and topography are largely responsible for this heterogeneity, influencing both dust and sand accumulation/erosion (Bridges et al. 2011). Finally, volcanic (pyroclastic), fluvial, glacial, and periglacial processes likely added a fine-component of sediment to specific terrains. In other areas, these processes were responsible for the destruction or resurfacing of an unconsolidated surface layer (Hartmann et al. 2001).

It is difficult if not impossible to generate a global regolith production model that incorporates these complicating factors. Rather, regolith thickness and production rates must be constrained locally, accounting for the specific geologic processes that have operated at that location through time. Here, we provide an analysis of regolith thickness and production rates in a region of southwestern Elysium Planitia on Mars (Fig. 1), accounting for local surface processes. This region was chosen as the final landing site for InSight (Interior Exploration using Seismic Investigations, Geodesy and Heat Transport), the 2018 Discovery class mission (Banerdt et al. 2013). Given the scale of the area that was originally under consideration for landing and the final size of each candidate landing ellipse (130 km by 27 km) (Golombek et al. 2014a, 2016b, [this issue](#)), this locality is uniquely covered by a broad set of high resolution imagery and topography data from the Mars Reconnaissance Orbiter's (MRO) High Resolution Imaging Science Experiment (HiRISE) and Context Camera (CTX). These include abundant 25 cm pixel⁻¹ resolution HiRISE orthoimages and

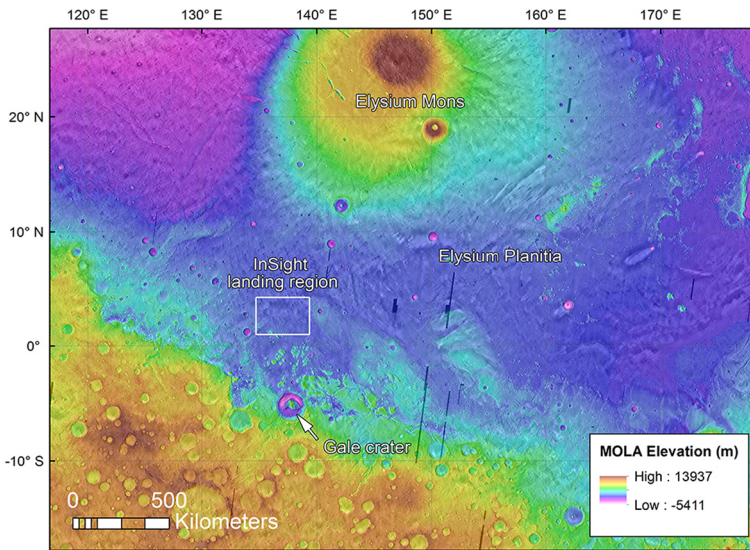


Fig. 1 Mars Orbiter Laser Altimeter (MOLA) gridded digital elevation map (463 m grid spacing) showing the location of the general InSight landing site region in southwestern Elysium Planitia

digital elevation models (DEMs) with 1 m elevation postings. We constrain regolith thickness, thickness variability, and production rates with implications for other Hesperian to Amazonian-age surfaces on Mars. Our analysis also provides a framework for understanding the surface processes that will be encountered by InSight and will be used for predicting the operational success of a specific lander instrument, namely the Heat Flow and Physical Properties Package (HP³) (Spohn et al. 2014).

1.1 The InSight mission and landing site

The InSight lander is scheduled to launch in May, 2018. It will constrain the interior evolution of Mars through seismology, heat flow and precision tracking measurements. The HP³ is a percussive drill or mole that will measure the heat flow of Mars by penetrating below the diurnal and seasonal skin depth. The desired depth of penetration to achieve this measurement is 5 m, with a minimum acceptable threshold of 3 m (Spohn et al. 2014). However, the HP³ requires an unconsolidated or very weakly bonded, sand to gravel-dominated soil that lacks greater than decimeter-scale, tabular rocks that can stop penetration. As a result, the presence of a loose surface regolith, formed partially through impact gardening and composed of poorly-sorted sand, gravel, and occasional cobble to boulder-sized clasts, is required for the HP³ to be successful.

The general landing region for InSight was chosen in southwestern Elysium Planitia (Fig. 1) based on low elevation and latitudinal constraints that relate to power and thermal considerations (Golombek et al. 2016b, this issue). Further investigation identified 22 possible landing ellipses located on Hesperian plains that appeared smooth in 100 m pixel⁻¹ global Thermal Emission Imaging System (THEMIS) infrared (IR) images and had low rock-abundance in thermal differencing remote sensing datasets. The final landing ellipse (E9) is centered at 4.4°N, 135.8°E (Golombek et al. 2016b, this issue) on the Early Hesperian Transition Unit (eHT) (Tanaka et al. 2014) (Fig. 2). Regolith production models that

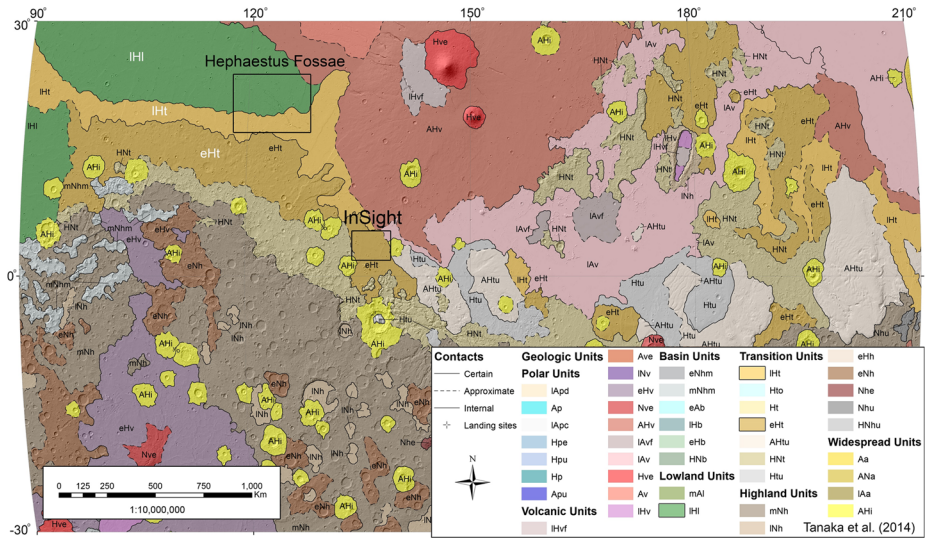


Fig. 2 Portion of the Tanaka et al. (2014) geologic map showing the location and geologic units at the InSight landing region. An outline of the Hephaestus Fossae region is also shown. Hephaestus Fossae exposes stratigraphy that is likely similar to what is beneath the landing site

account for the size-frequency distribution (SFD) of craters of a certain size on the surface suggest that Early Hesperian terrains should be capped by a regolith with order of 10-m-scale thickness (see Hartmann et al. 2001). These models have been generally confirmed by in situ rover (Spirit) observations of Hesperian cratered plains at Gusev crater (Grant et al. 2004; Golombek et al. 2006a). The floor of Gusev crater for instance is covered by an Early Hesperian-age basaltic plains unit (Tanaka et al. 2014). The unit remains largely unmodified, except by impact cratering and minor eolian re-working (Golombek et al. 2006a). Observations at the 210-m-diameter, 10 to 14-m-deep Bonneville crater confirmed that the Gusev plains are capped by an unconsolidated regolith that is at least 10 m thick (Grant et al. 2004; Golombek et al. 2006a). This upper unit is underlain by poorly sorted, (up to) 6-m-diameter boulder-rich material. No intact bedrock was observed.

Mapping during the InSight landing site selection process indicated that the Early Hesperian Transition Unit is most closely analogous in both surface morphology and near surface stratigraphy to the Gusev basaltic plains (Golombek et al. 2014b, 2016b, this issue). Multiple wrinkle ridges are visible across the landing region (Fig. 3), and degraded lobate landforms that are consistent with a lava flow morphology are visible along the northern edge, but outside of, the general landing region, including the final landing ellipse. Importantly, there is no evidence for fluvial, glacial, or periglacial modification in any of the candidate landing ellipses. Aside from the rims of impact craters and the margins of remnant highland terrains, regional slopes are low. Regolith development and re-working at this location on Mars is therefore most likely the result of impact gardening, dust accumulation, and eolian modification processes that followed the emplacement of Hesperian-age lavas. Our study therefore is most relevant to one end member surface type on Mars, the post Noachian (Hesperian-Amazonian) surface environment that was characterized by low rates of surface modification (Golombek et al. 2006b; 2014a). This kind of surface is arguably the most abundant of all terrains north of the planetary dichotomy and below the upper mid-latitudes. It is also common on the floors of topographic lows throughout the southern highlands (Tanaka et al. 2014).

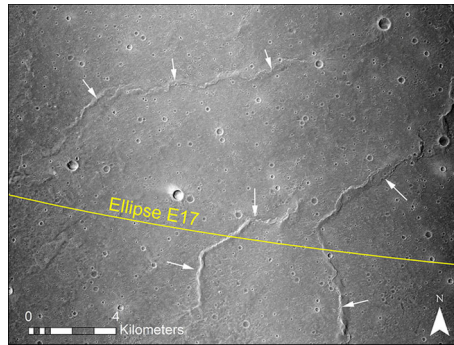


Fig. 3 Context Camera image (CTX) P15_006710_1843 displaying multiple wrinkle ridges on the Smooth Terrain in E17. Wrinkle ridges have been interpreted to be fault-propagation folds, in which slip on thrust faults at depth is accommodated by asymmetric folding in strong, but weakly bonded layered material (i.e., basalt flows) near the surface (e.g. Mueller and Golombek 2004). Wrinkle ridges are common across all Hesperian-age plains units (Tanaka et al. 2014), which has been used to argue that most are basaltic lava plains

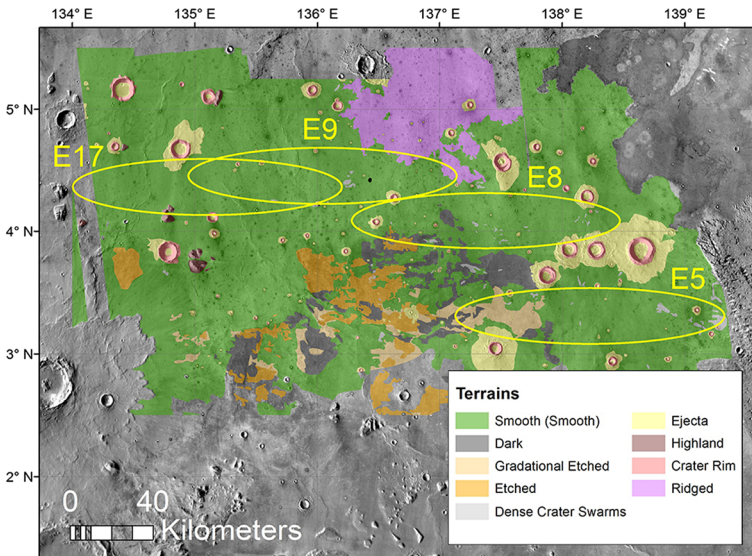


Fig. 4 Surface terrain map of the final four InSight landing sites (Golombek et al. 2016b, this issue) on a THEMIS daytime IR mosaic. The terrain map was produced for the landing site selection efforts using a near complete CTX mosaic at 1:40,000 scale. See terrain descriptions in the text. Landing ellipses are 130 km by 27 km oriented mostly east-west as shown. E9 is the landing ellipse selected for InSight

1.2 Terrains and Type Stratigraphy for the InSight Landing Region

Landing site selection and terrain safety evaluation for InSight involved a 4 year process of geologic mapping using CTX and HiRISE imagery. Golombek et al. (2014a, 2016b, this issue) provide details of the terrain mapping. Here, we summarize our terrain descriptions from that work for the final four landing sites (E5, E8, E9, E17) that were selected from the previous 22 candidates to provide a geologic and stratigraphic framework for this study. Figure 4 provides the terrain map. A generalized east-west orientation of

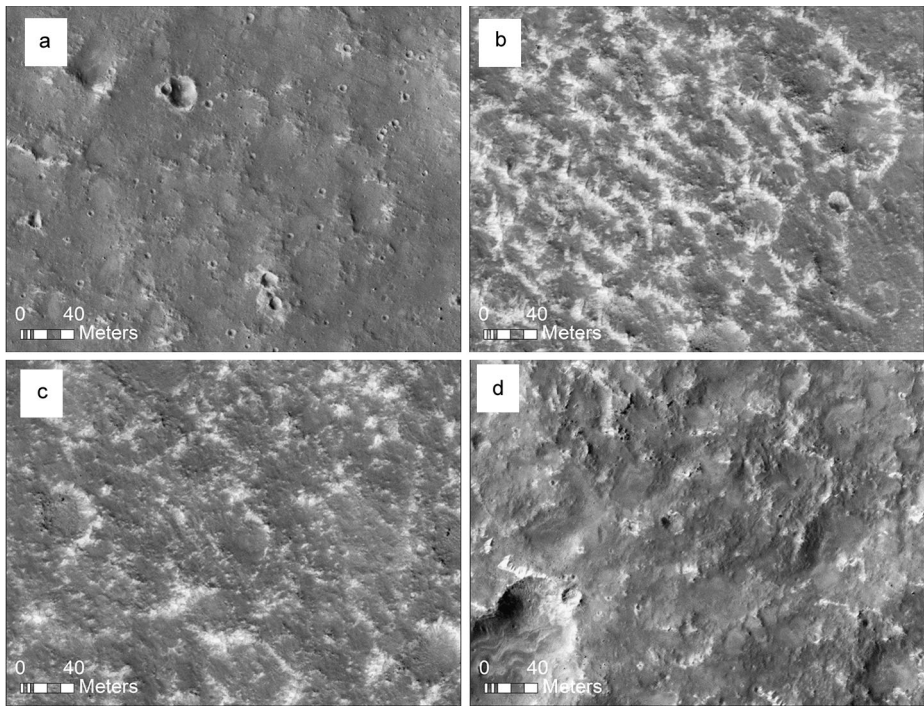


Fig. 5 Example HiRISE images displaying the four dominant terrain types in the InSight region. **(a)** Smooth Terrain has a muted surface texture and moderate albedo. **(b)** Etched Terrain has a rougher texture, exhibits high albedo bedforms, and a higher rock abundance. **(c)** Gradational Terrain represents a transitional terrain type between Smooth and Etched with fewer bedforms and rocks than Etched Terrain. **(d)** Dark Terrain is similar in morphology to Gradational Terrain but has fewer high albedo bedforms and fewer rocks. Note the population of small secondary craters with bright ejecta from Corinto crater in figure (a) (Golombek et al. 2016b, [this issue](#))

the 130 km by 27 km ellipses is shown here, which is representative of the ellipse orientations for the 2018 launch period. The map was produced at 1:40,000 using a near complete 6 m pixel⁻¹ CTX mosaic, georeferenced to a 100 m THEMIS Daytime IR mosaic basemap. Unique terrains were characterized first in CTX and described later in HiRISE based on their (1) albedo characteristics, (2) surface texture, (3) abundance of rocks, and (4) presence of bedforms.

The bulk of the region in the four ellipses is represented by a uniform terrain type called Smooth Terrain. Smooth Terrain is noted for its muted surface texture in CTX and HiRISE (Figs. 5a and 6), constant moderate albedo, and moderate THEMIS daytime IR signature. There are no obvious geomorphic (e.g. flow lobes) or thermophysical indicators that the Smooth Terrain is anything but a continuous geologic unit. The bulk thermal inertia of the Smooth Terrain is about 200 J m⁻² K⁻¹ s^{-1/2}, which is consistent with a surface composed of cohesionless fine sand size particles or a mixture of slightly cohesive soils (cohesions of less than a few kPa) that extends at up to a depth of 0.5 m depth (Golombek et al. 2016b, [this issue](#)).

The consistent appearance of the Smooth Terrain is interrupted by fresh impact craters that exhibit bright halos in the CTX imagery (Fig. 6). These same halos correspond with a dark daytime thermal signature and a bright nighttime signature, indicating that the ejecta

Fig. 6 CTX image D09_30814_1839 showing the higher relative albedo in the ejecta blankets of the larger Rocky Ejecta Craters (RECs) and eolian bedforms in the largest crater. The higher albedo is produced by bright eolian bedforms that are temporarily trapped between the rocks in the ejecta blanket and the crater rim. The rocky and sandy ejecta blankets on the larger RECs form an annulus that is approximately one crater diameter from the rim

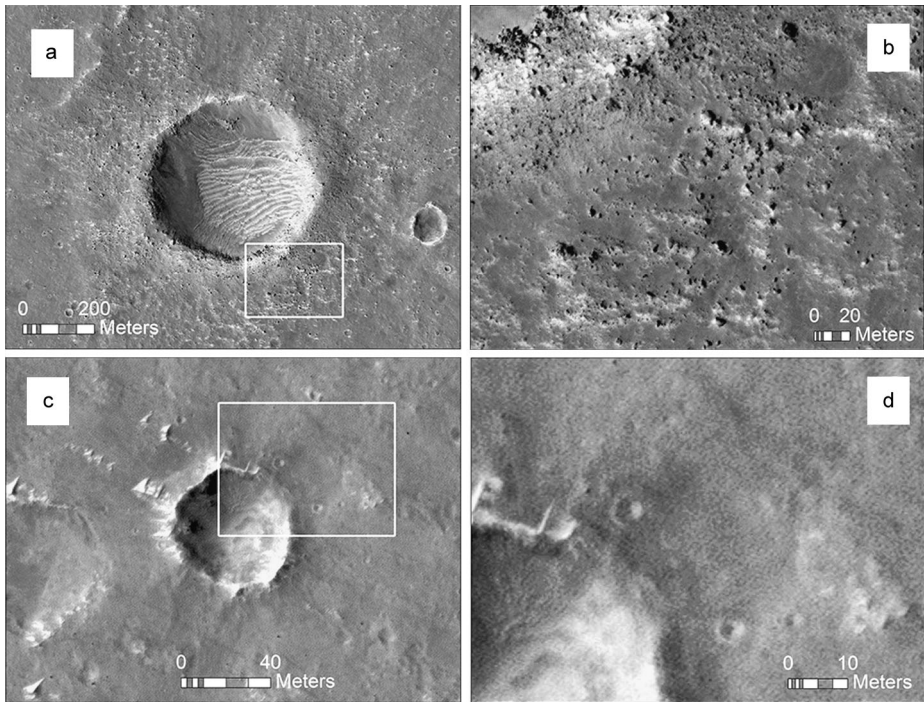
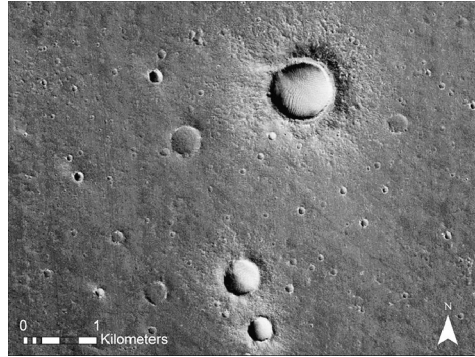
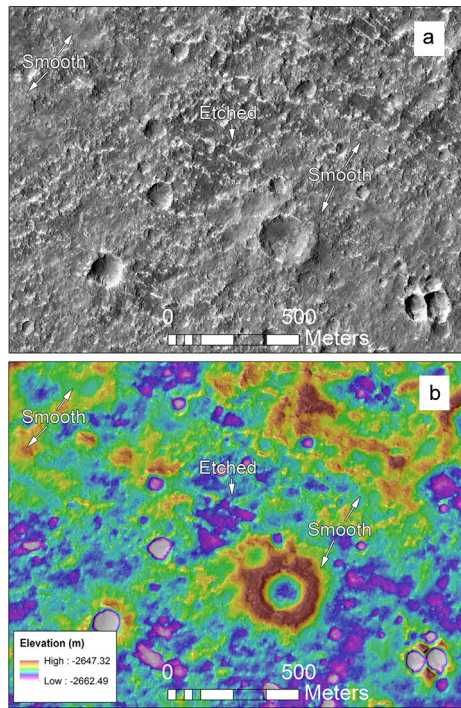


Fig. 7 HiRISE images display important differences in the rock abundance of rocky ejecta craters (RECs) and non-rocky ejecta craters (NRECs). (a) A 200 m diameter Class 2 REC showing a near continuous rocky ejecta blanket with bedforms. The maximum rock abundance (cumulative fractional area) in the ejecta of >200 m diameter RECs is approximately 30% near the rim and <10% at the ejecta edge. Image ESP_032660_1845. (b) Zoomed in view showing the size and abundance of the boulder-sized clasts in the ejecta blanket of (a). Bright bedforms are also visible. (c) Image showing a relatively fresh (similar to Class 3 REC), 50 m diameter NREC. Image ESP_035996_1835. (d) Zoomed in view showing a general lack of rocks in the one diameter annulus of this crater's continuous ejecta blanket

has a higher thermal inertia than the surrounding surface. HiRISE imagery over these halos reveal both bright eolian bedforms and abundant boulder-sized rocks that extend approximately 1 crater diameter from the crater rim (Fig. 7a and b). We interpret these rocks as ejected material from a rock-producing layer at depth. We use the term rock as a generic

Fig. 8 (a) HiRISE orthoimage ESP_035073_1840 and (b) the derived 1 m elevation posting DEM showing the morphologic characteristics of Etched Terrain. Etched is characterized by a patchy higher albedo relative to the more muted Smooth Terrain. The DEM reveals patchy topography, represented by multiple ~ 5 m deep topographic depressions. The rims of some impact craters appear as elevated pedestals over the surrounding Etched Terrain, suggesting surface deflation, likely by eolian erosion



description of what can be seen in the images, even though most are boulders. We refer to these craters throughout this study as Rocky Ejecta Craters (RECs). While this observation might initially argue against a loosely consolidated surface layer, further inspection during the landing site selection activities revealed that not all small, relatively fresh craters exhibit rocks in their ejecta (Fig. 7c and d) (Golombek et al. 2016b, [this issue](#); Warner et al. 2016). This initial observation led to the hypothesis that the smaller impacts were impacting into a (order of) meters-thick regolith that overlies the rocky layer and thus do not have rocks in their ejecta. We refer to this throughout as the regolith buffering effect.

Within the southern-most ellipses (E8 and E5), three additional terrain types were identified that exhibit a variety of albedo and textural characteristics. Coupled with observations of the Smooth Terrain, the Etched, Gradational, and Dark terrains provide insight into the subsurface vertical stratigraphy. Etched Terrain is characterized in HiRISE and CTX imagery by a relatively high albedo (Fig. 5b). In THEMIS IR data the Etched Terrain shows a variable thermal signature, showing both cool and warm daytime temperatures (Golombek et al. 2014a, 2016b, [this issue](#)). The etched surface texture is characterized by 10 to 100-m-wide, partially closed, <5 m-deep topographic depressions that are surrounded by remnants of Smooth Terrain. The depressions are commonly infilled with higher albedo bedforms and show a generally higher rock abundance (Figs. 5b, 8) (Golombek et al. 2016b, [this issue](#)). RECs that are brighter in Smooth Terrain still appear in the Etched and other terrain types, yet lack the same albedo and thermal contrast. Furthermore, some of these craters form resistant pedestals that are elevated by as much as 10 m above the patches of Etched Terrain. The most plausible hypothesis for the incomplete removal of Smooth Terrain and isolation of pedestal craters is by eolian deflation of loosely consolidated material at the surface. The higher rock abundance in the Etched Terrain might therefore represent a coarse lag or an ex-

posure of a rockier unit that is stratigraphically below the Smooth Terrain (Golombek et al. 2014a, 2016b, [this issue](#); Warner et al. 2016).

The interpretation for the Etched Terrain as a modified form of the Smooth Terrain is strengthened by the observation of transitional terrain types between them, called Gradational and Dark terrains (Fig. 5c and 5d). The Gradational Terrain has an intermediate rock abundance, elevation, albedo, and surface roughness relative to the Smooth and Etched Terrains. Gradational Terrain is named because it commonly exists as a gradational contact between the Etched and Smooth Terrains. Dark Terrain is noted for its low albedo in CTX imagery, cool THEMIS daytime signature, and warmer nighttime signature. The Dark Terrain also occurs as a transitional unit between the Smooth and Etched surfaces, yet it lacks the light-toned bedforms of the Etched and Gradational types. It has an overall lower rock abundance in comparison to Gradational and Etched terrains. We interpret the Dark Terrain as a similarly modified version of the Smooth Terrain where eolian deflation of overlying higher albedo material has exposed a lower albedo, possibly more indurated surface. This is consistent with its generally higher thermal inertia. Collectively, these terrain observations represent only surficial variations in the textural and physical characteristics of the Hesperian plains in this region and support the presence of an unconsolidated surface unit or regolith that may overlie a rockier unit.

2 Methods

2.1 Size-Frequency Distribution of RECs

In the absence of direct stratigraphic observations along exposures or cuts, fresh impact craters and their ejected material represent the primary window into the subsurface. Dozens of HiRISE images were targeted and acquired through the landing site selection process over the final four ellipses (Golombek et al. 2016b, [this issue](#)). For this analysis we mapped and recorded the diameter of all RECs in 44 HiRISE images using ArcMap 10.2, which includes 7988 craters within the four ellipses (Fig. 9). Using depth of excavation versus crater diameter relationships (e.g. Melosh 1989; Hermalyn and Schultz 2011; and Grieve et al. 1981), the diameter of RECs can be used to evaluate the depth to the rocky unit as well as a cutoff diameter at which rocks stop appearing in the ejecta. A similar method has been used by other authors (e.g. Thompson et al. 1979; Bart and Melosh 2010; Catling et al. 2012) to characterize the near surface stratigraphy of the Moon and Mars, including the original lunar study by Shoemaker and Morris (1969).

The cutoff diameter serves as a proxy for regolith thickness based on the assumption that a lack of ejected rocks indicates impact into finer-grained or less indurated material. The appearance of boulder-sized clasts further suggests that the regolith has been punctured, and a rocky unit has been accessed. The excavation depth of ejecta within the continuous blanket of a simple crater is approximately 0.1 times the transient crater depth (Melosh 1989). The transient crater diameter is 0.84 times the diameter of the final crater, indicating that ejecta is sourced from 0.084 times the crater diameter. Research supporting this suggests that the depth of excavation varies from 0.06 to 0.09 depending on the angle of impact and on properties of the impactor and target. Vertical gun tests into colored, layered sand indicate that ejecta in the continuous ejecta deposit comes from about 0.06 times the final crater depth (Stoffler et al. 1975). A review of terrestrial impact craters by Grieve et al. (1981) indicates that the depth of excavation for simple craters is about 0.07–0.09 times the final crater diameter. Vertical gun experiments using different impactors show that the depth of

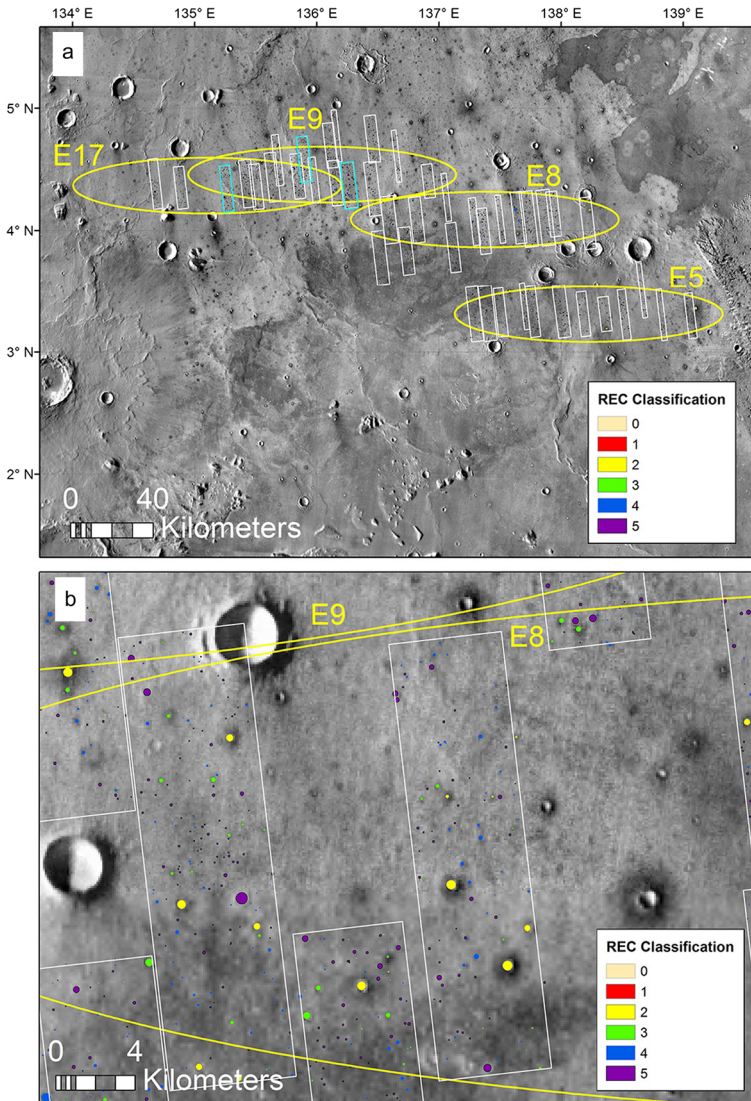


Fig. 9 THEMIS daytime IR mosaics displaying (a) the HiRISE image coverage before the second landing site downselection (Golombek et al. 2016b, *this issue*) and (b) REC classification map over the final four landing ellipses. The *color code* for the different crater morphologic classes is used throughout the analysis. The three blue images in (a) are the locations of the DEMs used in this study. Background is THEMIS daytime thermal image mosaic (100 m pixel⁻¹) showing the dark annuli of the higher inertia rocky ejecta craters

excavation is around 0.06 times the final crater diameter for polyethylene and nylon impactors and increases to 0.07 for pyrex, aluminum, titanium and steel impactors (Hermalyn and Schultz 2011). Finally, Schultz and Anderson (1996) show that the excavation depth is reduced uprange and downrange for oblique impacts. Here, we assume that the continuous ejecta blanket is derived from a depth of 0.084 times the diameter as reported by Melosh

(1989), but discuss variations in the depth of excavation from 0.06 to 0.09 times the final crater diameter.

Because it is impossible to visually survey and measure all RECs to determine depth of excavation individually, we use crater cumulative and incremental size frequency distributions (SFD) to constrain the diameter at which the RECs decrease in abundance and eventually disappear. In the absence of a regolith and/or surface processes that removed craters as well as rocks from the ejecta, a cumulative size frequency histogram that only includes RECs should generally follow a crater production function. Furthermore, even in the presence of surface processes that can modify or eventually destroy craters and rocks, if these processes operated at low rates, the rocky craters may remain over long timescales. RECs in the InSight landing region range from 10 m to 1.4 km in size. Therefore, as an example from a cumulative SFD histogram over this diameter range, a $\log N$ (cumulative number of craters per area) versus $\log D$ (diameter) plot of RECs should follow a crater production slope if all impact events struck a rock-producing unit and if these rocky craters were not obliterated over time. In reality, surface processes operate to destroy small craters and the rocks in their ejecta.

It has been suggested that at some diameter that is dependent on surface age and local surface modification, a steady state or equilibrium is reached where craters below a certain size are destroyed at or near the same rate as they are produced (e.g., Melosh 1989; Hartmann 1984). This may be due to a combination of processes on Mars that include impact gardening and some component of eolian modification. On a $\log N$ vs. $\log D$ plot the slope of the steady state equilibrium function is close to -2 (Hartmann 1984; Hartmann 2005). But, under more vigorous surface modification, the size-dependent destruction of small craters results in SFDs whose slopes are often lower than the equilibrium model (Golombek et al. 2014b; Fassett and Thomson 2014; Xiao and Werner 2015). Therefore, even in the absence of a regolith, the slope of the cumulative SFD histogram should decrease and may reach, approach, or go lower than the equilibrium function at smaller diameters as a result of surface processes. Therefore, a cumulative SFD plot of our REC dataset in the absence of a regolith should include a steeper production branch for larger crater diameters and a shallower branch over a range of smaller crater diameters. However, we hypothesize that if a regolith is present then a SFD that tracks only RECs should exhibit a decrease in slope that exceeds that represented by both production and the influence of small crater modification at some cut off diameter that is reflective of the maximum regolith thickness. Here we compare the SFD of all rocky ejecta craters to the Ivanov (2001) production function and the Hartmann (1984) equilibrium functions accounting for the effects of small crater degradation.

2.2 Size-Frequency Distribution Roll-off and Crater Obliteration

Mechanisms that generate roll-offs or slope kinks in the crater SFD besides the regolith buffering mechanism and surface processes include human counting errors and limits in the resolution of the dataset. For this study each impact crater was mapped and its morphology evaluated by two or more individuals. The lead author was involved with the final confirmation of the crater mapping and the morphologic classification. A conservative resolution limit for identifying an object in HiRISE is approximately 3 to 4 pixels. The range of pixel scales in our data set is approximately 25 cm to 30 cm (McEwen et al. 2007) indicating that craters and rocks are identifiable above scales of 0.75 m to 1.2 m. However, as few as 1 to 2 pixels can be used to visually identify shadows that occur in patterns that are consistent with ejected blocks (i.e. in a continuous annulus around the crater), particularly when

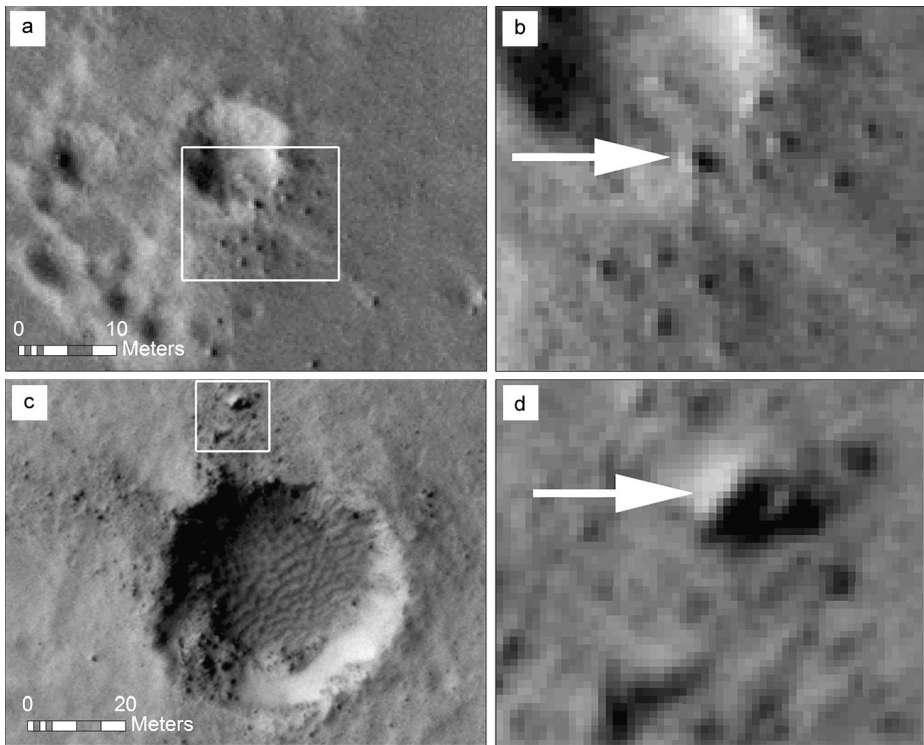


Fig. 10 HiRISE images displaying the rock abundance and rock sizes in the ejecta blankets of relatively small RECs. (a) Example of one of the smallest RECs in our dataset (10 m). (b) Zoomed in image of the 10 m REC showing 0.5 to 0.75 m diameter rocks that are noted by shadows that are 2 to 4 pixels across. (c) Example 50 m diameter REC. (d) Image shows the typical maximum block size associated with a 50 m crater. The boulder is 3 m wide by 5 m long and casts a large shadow that is many pixels across. The rock abundance around this crater is discontinuous within a one diameter annulus, measured outward from the crater rim. This is unique relative to larger >200 m diameter RECs that have rocks distributed throughout their continuous ejecta blanket

the terrain contains no other roughness elements that cast shadows. This is particularly the case for RECs that superpose the Smooth Terrain. The RECs evaluated here are >10 m in diameter, and the majority are between 30 m and 200 m. The craters themselves are well within the resolution limit for identification in HiRISE. From inspection of all 44 HiRISE images, 0.5 m to 5 m diameter rocks create shadows that are >2 pixels wide across the range of solar illumination angles (Fig. 10). The smallest RECs are 10 m in diameter and have boulders that are at most 0.5 to 0.75 m in size (Fig. 10a, b). At solar incidence angles of 30° to 55° that are typical of the HiRISE images in our dataset, these rocks cast shadows that are 2 to 4 pixels wide. The maximum block size for a 50-m-sized crater in our dataset is approximately 3 to 5 m in diameter (Fig. 10c, d), which casts a shadow that is roughly 5 to 6 pixels in length. For comparison, the mean block size in the continuous ejecta at Bonneville crater (210 m diameter) on the Gusev ridged plains is 2.95 meters, measured from rover-based observations (Grant et al. 2004). Rocks approaching 6 m in diameter were identified along the interior of the rim. Furthermore, the size of rocks around craters has been studied extensively on the Moon (Shoemaker and Morris 1969; Moore et al. 1969; Cintala and McBride 1995; Bart and Melosh 2007; Basilevsky et al. 2013). From these lu-

nar observations, Melosh (1989) reports a relationship between the maximum block ejected from a crater and its diameter; $B = KD^{2/3}$, where B is the block size, D is the crater diameter (in meters), and K is a constant. Data reported in Moore (1971) suggests that K is typically 0.1 to 0.3 for primary lunar craters. For a 10 m diameter crater, similar to the smallest REC in our dataset, the maximum block size should be 0.5 to 1.4 m depending on the value of K . At 50 m, the maximum block size is approximately 1.4 m to 4.0 m. The maximum block-diameter relationship therefore predicts a similar maximum block size relative to our observed maximum block sizes around the RECs. We conclude that for the bulk of our REC dataset, meter-scale ejected rocks on fresh > 10 m-sized craters should be readily observable at HiRISE resolution across all relevant incidence angles.

To evaluate the rates of surface processes in this region we first classified the morphology of each REC on a relative scale of 1 to 5 where 1 represents the freshest, rocky ejecta craters and 5 represents the most degraded rocky ejecta craters. Table 1 provides the specific morphometric characteristics for the RECs. Section 3.2 describes our morphologic and SFD observations of these craters. We do not include the more degraded and more numerous impact craters that lack rocks in their ejecta. The classification is based on our geomorphic analysis of the entire crater with HiRISE imagery, including the characteristics of the rim, interior slope, floor, and continuous ejecta blanket (Table 1). The classification is supported by comparisons to measured morphometry using HiRISE DEMs with 1 m elevation postings. The HiRISE DEMs were produced for the landing site assessment (Golombek et al. 2016b, this issue; Fergason et al. 2016, this issue) using the SOCET-SET stereogrammetry program and standard United States Geological Survey (USGS) methods (Kirk et al. 2008; Fergason et al. 2016, this issue). We chose to evaluate three DEMs in the selected landing ellipse E9 that encompass 716 RECs (Fig. 9a). For each crater, 4 topographic profiles were constructed to measure a mean depth and diameter. Rim height relationships were also evaluated by measuring the elevation of the rim at 8 points around the crater as it compares to the elevation of the surrounding plains.

The morphologic classification scheme was used to break the craters into populations based on inferred degradation state. The assumption here is that a crater's morphometry is reflective of the timescale over which it was exposed to surface processes. In other words, Class 1 craters are considered here to be collectively younger than Class 2 craters, which are also younger than Class 3 (and so on). This assumption is invalid when considering craters with different degradation histories, as may be the case when comparing craters that span multiple geologic units, latitudes, or elevations. However, the unusually large REC dataset here comes from a spatially restricted region of Hesperian plains where the diversity of surface processes has been limited to impact cratering and eolian modification (Golombek et al. 2016b, this issue). These processes are considered here to have operated at steady rates since the Hesperian.

Given the key assumption that morphology reflects age, we break our crater classes into progressively younger groups to determine their size frequency distribution and thus timescales of degradation. For example, the cumulative SFD of all craters in Class 1 to 5 (all RECs in the region), plotted against the chronology and production functions of Mars (Hartmann and Neukum 2001; Ivanov 2001; Hartmann 2005), should provide the maximum timescale over which craters preserve rocks in their ejecta. A SFD plot of craters from Class 1 to 4 however reveals the timescale over which this younger subset of rocky craters formed, after the time of formation of Class 5 craters. The youngest subset we use here includes the grouping of Class 1 with 2 craters, due to the limited number of Class 1 craters in our dataset.

Table 1 Descriptive morphologic classification scheme for the RECs

Class	Crater morphology	Ejecta characteristics
1	<ul style="list-style-type: none"> ● rim defined entirely around crater ● rocks eroding into crater basin from rim, rocks exposed on crater wall ● few bedforms present in crater floor ● no smooth infill present ● no impact craters present on crater floor 	<ul style="list-style-type: none"> ● completely surrounds crater ● continuous blanket approximately one diameter of crater ● bedforms prominent throughout ejecta blanket ● little collection of sediment between bedforms
2	<ul style="list-style-type: none"> ● rim defined around entire crater ● rim intermittently eroded or rounded ● rim exhibits few to no impact craters ● rim exhibits pronounced albedo, due to bedforms trapped against rim ● no smooth infill present ● bedforms present throughout crater floor 	<ul style="list-style-type: none"> ● completely surrounds crater, covering 75% of annulus ● blanket approximately one diameter of crater ● bedforms present throughout ejecta blanket ● ejecta may exhibit superposing impact craters
3	<ul style="list-style-type: none"> ● rim defined around almost entire crater ● rounded rim with interior alcoves ● rim exhibits few impact craters ● rim exhibits pronounced albedo ● smooth sediment infill present, but does not cover entire crater floor ● infill may exhibit impact craters or large rocks eroding from rim ● bedforms partially exposed on crater floor 	<ul style="list-style-type: none"> ● ejecta becomes discontinuous, cover 50–75% of annulus ● annulus of ejecta around crater is approximately one half crater diameter or more ● bedforms intermittently present throughout ejecta blanket ● collection of smooth material between distal bedforms and rocks, causing irregular ejecta patterns ● ejecta exhibits superposed impact craters
4	<ul style="list-style-type: none"> ● rim may be eroded or degraded in multiple places forming a notch or series of alcoves ● rim exhibits impact craters ● rim exhibits pronounced albedo due to bedforms ● smooth infill completely covers crater floor. ● Infill retains impact craters with sharp rims. ● few to no bedforms present in basin of crater 	<ul style="list-style-type: none"> ● intermittently surrounds crater, covering 25–50% of annulus ● blanket extends less than half diameter of crater ● bedforms present close to rim of crater ● ejecta blanket is mostly smooth ● ejecta exhibits superposed impact craters
5	<ul style="list-style-type: none"> ● degraded rim with multiple notches and alcoves ● rim often completely eroded in places ● rim exhibits impact craters ● elevated rim segments maintain high albedo compared to the most degraded craters ● crater is entirely filled with smooth infill sediment ● sediment fill exhibits impact craters with sharp rims ● no bedforms present in basin of crater 	<ul style="list-style-type: none"> ● not continuous around crater, covers <25% of area in annulus ● distance from crater rim less than half diameter of crater ● few bedforms present ● ejecta blanket is mostly smooth ● ejecta exhibits superposed impact craters

2.3 Mapping of Non-rocky Ejecta Craters

If there is an onset diameter below which craters do not excavate rocks, then a significant portion of smaller fresh craters should lack rocks in their ejecta blanket. To test this, we mapped all ≥ 30 m size non-rocky fresh craters (NRECs) in the 3 HiRISE images that corre-

spond with our DEMs (Fig. 9a). The NRECs were first visually classified and then characterized with the DEMs to ensure their morphologic similarity to the relatively fresh, Class 1 to 5 RECs. We do not include non-rocky craters that are more degraded than the Class 1 to 5 examples. We hypothesize that if a roll off in the slope of the SFD of the RECs is the result of regolith buffering and not some degradational surface process, then adding the morphologically similar NRECs to that dataset should increase the slope of the SFD. However, if crater obliteration plays a major role in destroying smaller craters systematically across the region, then there may be very few fresh NRECs and a significant roll-off would still exist regardless of their inclusion in the dataset.

2.4 Regolith Thickness from Crater Morphology

To test our results from the analysis of the distribution of the RECs we used an independent method for estimating regolith thickness that is based on crater morphology. Loosely consolidated, finer-grained regolith should have a significantly lower material strength than intact or even brecciated bedrock. Energy from an impacting bolide as it collides with a target is transferred to the excavation of that material (Quaide and Oberbeck 1968; Bart et al. 2011; Senft and Stewart 2007). However, when a bolide impacts a material of higher strength, some energy is required to initially fracture and then disaggregate the rock before it can be excavated. The energy transferred to the actual excavation and block ejection process is therefore lower for an impact into solid bedrock as compared to regolith (for an impacting body of equal energy). In two-layer experiments that model regolith over bedrock, central mound, flat-floored, and concentric craters have been produced for impactors below a specific energy threshold where target strength controls the resultant crater morphology (Quaide and Oberbeck 1968; Bart et al. 2011; Senft and Stewart 2007). As the impactor enters the target, and if the energy required to fragment and excavate the bedrock is insufficient to continue the crater forming process, a mounded or flat floor is preserved. Concentric or nested craters represent those craters that formed by excavation of both the overlying weak regolith and the underlying stronger layer. Simple bowl-shaped morphologies dominate in these experiments where craters form solely in a lithologically and structurally uniform stratigraphy or where the energy of the impactor exceeds the threshold where target strength is no longer the controlling factor. Most flat-floored, mounded, and concentric crater morphologies occur at $D = 50$ m to 200 m on the lunar mare (Quaide and Oberbeck 1968).

For concentric craters, the ratio of the apparent diameter D_A measured from rim crest to rim crest of the primary outer crater, to the diameter of the inner nested crater D_F (D_A/D_F) is related to the ratio of D_A and regolith thickness t (D_A/t) (Quaide and Oberbeck 1968; Bart et al. 2011). The D_A/t ratio at each morphologic transition varies by $\pm \sim 1$ due to uncertainties in target strength and impact angle. Equation (1) solves for t using the experimental data and measured crater parameters (see discussion in Bart et al. 2011). The non-dimensional empirically-derived k is a ratio of the actual crater diameter D_T as it is measured at the level of the ground surface to the apparent crater diameter D_A (D_T/D_A). This value is commonly given as 0.86 for simple bowl-shaped craters on the lunar surface (Quaide and Oberbeck 1968; Bart et al. 2011). The angle of repose α for loose material under gravity is also required. From a subsequent survey of lunar craters using LROC data, Bart (2014) demonstrated that Eq. (1) is only useful for calculating regolith thickness where the ratio of D_F/D_A is between 0.2 and 0.7 and within a range of 20 m to 100 m for crater diameter. At lower or higher values there is no identifiable relationship between these parameters and the thickness of the regolith.

$$t = (k - D_F/D_A)D_A \tan(\alpha)/2 \quad (1)$$

The results of the Quaide and Oberbeck (1968) work suggest that the development of these crater morphologies is dependent on contrasts in the target strength and not parameters that are unique to the planetary body (e.g. gravity). Thus, Eq. (1) for concentric craters should be generally transferable to Mars for craters below a specific size threshold. For this work, we scanned all 44 HiRISE images in the InSight landing region to visually identify morphologic transitions that are consistent with concentric craters. Flat-floored or central mound morphologies could not be distinguished from craters that were partially infilled by eolian material. Where appropriate we used Eq. (1) to estimate regolith thickness. For those craters that also correspond with HiRISE DEMs we determined the depth from the surface to where the interior inner crater is expressed.

2.5 Regolith Thickness Variation

Local variations in regolith thickness may exist in the InSight region where the landscape morphology or unique surface processes favor or prohibit significant accumulation. For example, we hypothesize that the Etched Terrain developed in response to eolian stripping of a smoother cover (the Smooth Terrain). This hypothesis implies that the regolith is locally thin at locations of the Etched and transitional terrain types (Gradational and Dark). The identification of km²-scale spatial variations in regolith thickness has implications for understanding the processes that influence regolith production, modification, and continuity across Mars. Furthermore, this analysis is potentially an important predictive tool for penetration of the HP³ mole towards understanding the regolith thickness at specific points inside the final landing ellipse.

We evaluate thickness heterogeneity in two ways. First, we generated a subset of the REC crater statistics for those craters that impacted into Smooth Terrain versus those craters that impacted into Etched, Gradational, or Dark terrains. From these data we constructed terrain specific SFD plots to compare variations in the diameter at which the RECs disappear. Second, we generated a crater density map to visualize clusters or dispersed patterns in our dataset that might indicate local variations in the depth to the rock-producing unit. To do this we converted each digitized crater shape to a centroid point in ArcMap. The point data was then used to generate a kernel density map. The kernel density tool calculates the number of points per defined unit area and generates a raster with an assigned grid spacing. Here we display our density data in units of craters km⁻². The search radius or neighborhood used to calculate the density was set to the default radius. The default radius is assigned by ArcMap using the spatial configuration and number of data points, to reduce the impact of point outliers. In this instance, the default radius calculated by ArcMap was ~2 km. Edge effects occur where the density calculation was carried out in an isolated HiRISE image as opposed to a mosaicked set of images. At the edge of an image, the search seeks points beyond the image boundary, at locations of no data. To limit the visual and statistical impact of the resultant low density values beyond and at the edge of the image, we clipped the data to display only those values that fall within the immediate boundary of the HiRISE image. Low density edge effects still exist in our data, within a few hundred meters of each image boundary. The width of these low density regions is variable along the perimeter of an image and is dependent on the proximity and number of data points at the immediate edge of the image. If non-random secondary cratering plays a minimal role in generating rocky craters, spatial clusters of RECs might indicate a locally thin regolith. Kernel density maps were constructed at specific diameter bins and using specific crater morphologic classes to evaluate whether clusters or dispersed patterns can be attributed to non-random processes like secondary cratering.

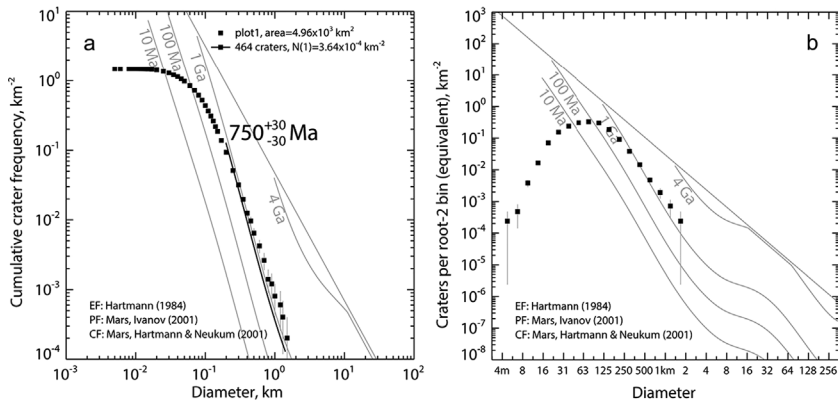


Fig. 11 Size frequency distribution plots for all RECs in the dataset, excluding Corinto secondaries (Class 0). **(a)** Cumulative crater size-frequency distribution plot with pseudo-log binning (Michael and Neukum 2010). A fit to the Mars chronology function of Hartmann and Neukum (2001) provides a model age for all RECs >200 m in diameter of ~ 750 Ma. *Error bars* on the age represent model age errors that are related to Poisson counting statistics and do not represent known uncertainty in mapping and interpreting the RECs. The distribution rolls off at $D < 200$ m and flat lines below 30 m. **(b)** Incremental crater size-frequency distribution plot with root-2 binning. The number of craters decreases below the production function (i.e. rolls over) at $D < 200$ m

3 Results

3.1 Size Frequency Distribution of RECs

Initial mapping of the RECs revealed a general lack of rocks in the ejecta blankets of morphologically fresh craters at diameters < 50 m (Fig. 7). Using the Melosh (1989) maximum depth to excavation relationship of 0.084 times the diameter of the crater, and assuming a vertical impact, rocks in the continuous ejecta blanket are ejected from a depth of 4.2 m for a 50 m crater. For the minimum reported excavation relationship of 0.06 (Hermalyn and Schultz 2011) and the maximum of 0.09 (Grieve et al. 1981), the values are 3 m and 4.5 m respectively. Craters below this size threshold that do not excavate rocks provide an upper limit on regolith depth. This first order observation suggests that a meters-thick regolith exists across the InSight landing region. In addition, THEMIS images initially indicated that there are few rocks in the ejecta blankets of >2 km-sized craters. Further analysis of HiRISE and CTX imagery across the region confirmed this observation (Golombek et al. 2016b, this issue). This suggests that the strong rock layer from which the rocky ejecta is sourced is less than 200 m thick with weaker sediments beneath.

Figure 11 displays the cumulative and incremental SFD plots for all Class 1 to 5 RECs across the 4 ellipses. At bin sizes >200 m diameter the slope of the SFD closely follows a crater production function. However, the plots illustrate a large slope reduction in the SFD at approximately $D < 200$ m, dipping well below both the production and equilibrium functions. The slope flat-lines on the cumulative plot and rolls over on the incremental plot at $D < 30$ m, indicating that there are almost no <30 m-sized RECs in this region. We therefore conclude that some process is controlling or preventing the formation and/or preservation of RECs below this size threshold.

A fit to the Mars chronology function (Hartmann and Neukum 2001) for the $D > 200$ m diameter portion of the curve provides a model age of $750 \text{ Ma} \pm 30 \text{ Ma}$. The near production

distribution of this population suggests that any impact that generated a > 200 m diameter crater within the last 750 Ma impacted into a rock-producing unit. The data also suggest that any crater of this size at this location that is < 750 Ma in age still preserves visible rocks at the resolution limit of HiRISE in its ejecta blanket, providing an upper limit on the timescale of rock preservation and degradation.

3.2 Crater Degradation and the Size Frequency Distribution Roll-Off

Figure 12 shows a HiRISE orthoimage and DEM example of Class 2 to 5 craters. This classification scheme is used to assess whether crater/rock degradation is responsible for some component, if not all, of the SFD slope reduction at $D < 200$ m. Class 1 craters are extremely rare in the region. By our definition, Class 1 craters represent the idealized pristine morphology of a simple crater (Fig. 13a) (Table 1). A Class 1 crater has a sharp and continuous rim, bowl-shaped interior, no interior eolian bedforms or thick dust infill, and rocks in a one crater diameter annulus around the crater rim. As an additional classification, we used the albedo of the area around the crater to indicate a recently formed crater. Fresh craters with before and after orbital images are identified by dark splotches that represent impact blast zones where dust has been removed from the surface, exposing lower albedo, likely basaltic material (Dauber et al. 2013). Over some timescale, on the order of ten years, the blast zone slowly accumulates dust until it disappears (Daubar et al. 2016). An obvious albedo contrast caused by a fresh strike was only identified for one REC. Other Class 1 RECs show lower albedo rocks and debris in their ejecta blanket (Fig. 13a) but lack the appearance of a blast zone.

Young, < 2 Mya secondary crater chains from Corinto crater are ubiquitous across this region; some secondaries from Zunil are also present (Preblich et al. 2007; Bloom et al. 2014; Golombek et al. 2014c; Hundal et al. 2017). It is therefore difficult to confirm whether all small, fresh craters are primary craters. There is likely significant uncertainty in evaluating the SFD of Class 1 craters. Class 0 RECs are identified here as known Corinto secondaries and are excluded from all SFDs presented in this work. Corinto secondary craters are noted across the four landing ellipses for their characteristically bright, lobate ejecta (Fig. 14), occurrence within and on the periphery of north-northeast trending chains that point back to Corinto (Bloom et al. 2014), collectively low thermal inertia signature, pristine appearance with little or no eolian infill, and shallow depth profiles relative to their diameter (Dauber et al. 2016; Golombek et al. 2016b, this issue). We identified 632 rocky ejecta Corinto secondary craters in the 44 HiRISE images. Their diameters range from ~ 10 m to 70 m, with a mean of 25 m. However, a majority of the rocky Corinto secondaries do not show rocks completely around the crater. Rather, only a few rocks are scattered down-range. It is not clear in some cases whether these rocks were truly ejected from the subsurface given the expected lower impact velocities compared with primaries or are preserved remnants of the impacting material.

Class 2 craters (Fig. 12a, b) are noted for their near continuous rocky ejecta blankets, bowl-shaped interiors, limited eolian infill, and occasional, small superposed impact craters (Table 1). In this case, the infill is dominated by ripples and larger dunes. This indicates that craters are important sediment traps for sand-sized particles (Fig. 7a). Rocks in the ejecta of Class 2 craters also trap sand-sized materials (Fig. 7b). This creates the appearance of higher albedo ejecta when observed in lower resolution CTX imagery (Fig. 6).

Progressing from Class 3 to Class 5 (Fig. 12c–h), the craters exhibit progressively more modification where: (1) the rims become less continuous, displaying notches or breaks along their circumference, (2) their interiors shallow and become more infilled, (3) the interior

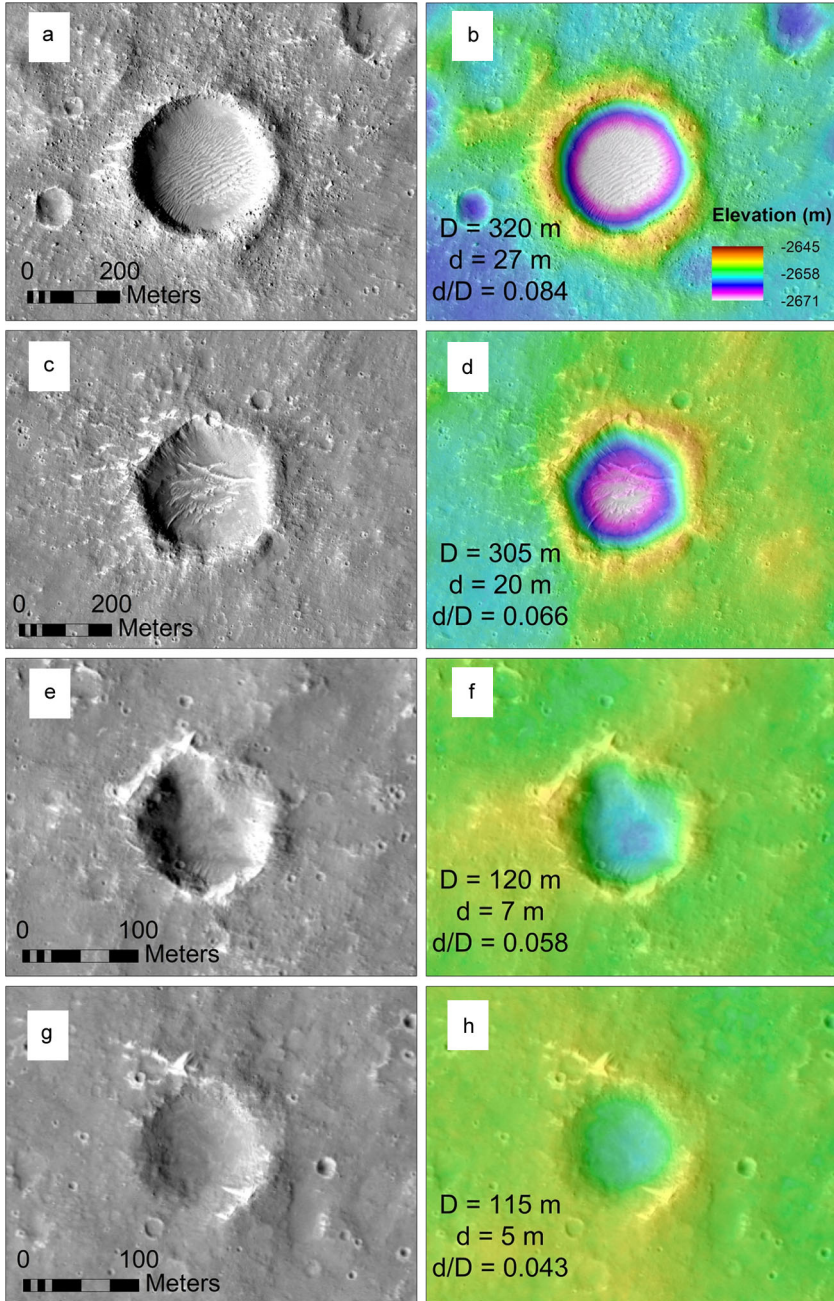


Fig. 12 HiRISE orthoimage ESP_037961_1845 and the stereo-derived 1 m elevation posting DEM displaying the different morphology classes of the RECs. Plates (a) and (b) represent a Class 2 crater, plates (c) and (d) show a Class 3 crater, (e) and (f) are of a Class 4 crater, and (g) and (h) exhibit a Class 5 crater. The elevation *color bar* shown in (b) is representative of all 4 DEM plates. Depth and diameter data for these craters are also shown

Fig. 13 HiRISE images showing Class 1 craters. (a) Image ESP_040124_1845 showing a ~60 m diameter fresh crater that has excavated dark boulders. (b) Image ESP_036405_1850 of a ~20 m diameter fresh crater that lacks boulder-sized clasts in its ejecta

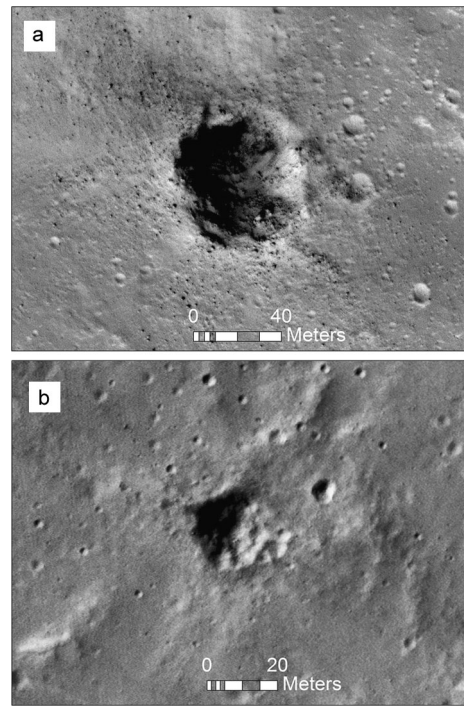
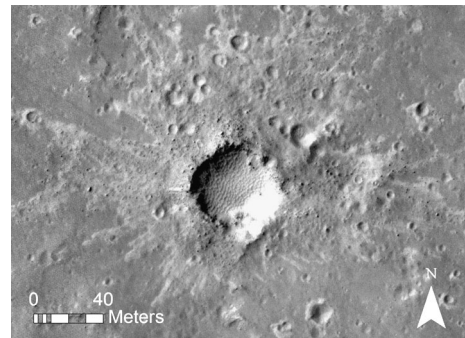


Fig. 14 HiRISE image ESP_034506_1835 showing a large Corinto secondary crater. This crater, at 40 m in diameter, has excavated a handful of meter-sized rocks and exhibits the characteristically bright ejecta associated with Corintos. Bedforms have also begun to fill the interior



bedform morphology changes to a smoother surface, (4) the bedforms within the ejecta blankets become trapped against the crater rim, (5) superposing impact structures appear within the ejecta, on the rim, and on the fill, and (6) the rocks in the ejecta become less pronounced and are more discontinuously distributed. However, by our definition, the Class 5 crater is the most-degraded class of crater to still exhibit rocks in its ejecta at the resolution limit of HiRISE. Therefore, even Class 5 craters represent a relatively fresher class of crater when compared to the older non-rocky degraded craters that dominate the crater population.

Figure 15 presents the morphometric data of a subset of RECs obtained from three HiRISE DEMs (see Fig. 9 for the location of the DEMs), including depth versus diameter and rim height versus diameter. The data show that there is a progressive shallowing of craters with increasing morphologic class. Similarly, rim height decreases progressively with increasing morphologic class. In both cases, depth and rim height show a linear rela-

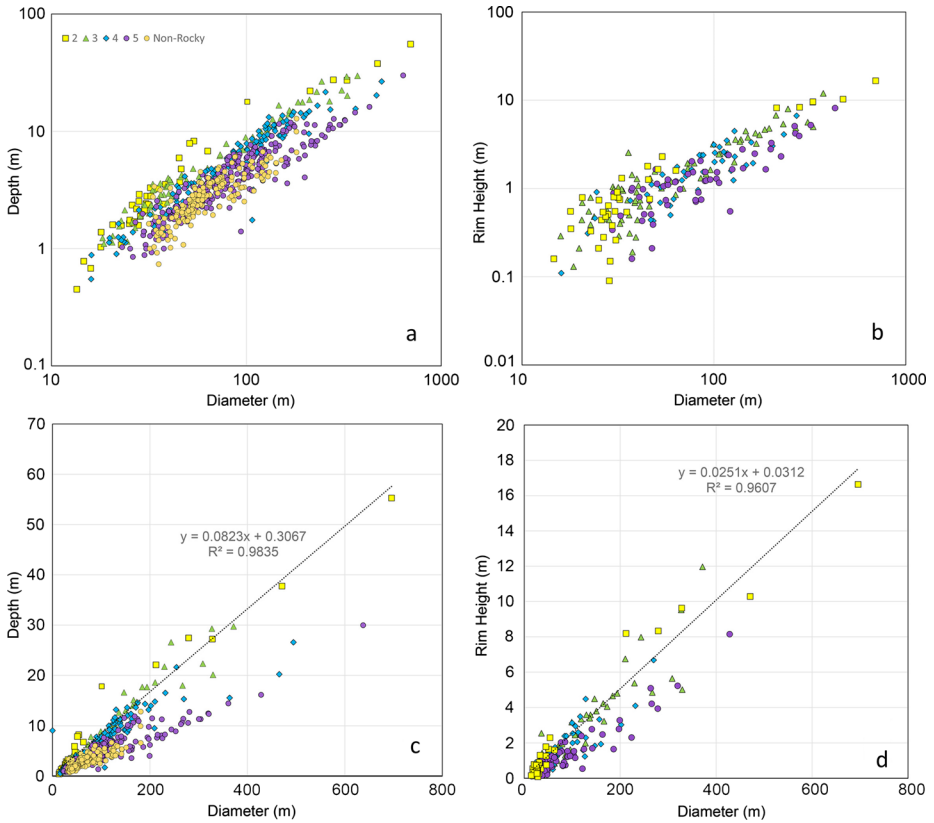


Fig. 15 Morphometric data from HiRISE DEMs for the different crater classes, excluding Class 1. Class 1 craters are rare and exhibit a broad range of depth and rim height characteristics that might suggest contamination by secondaries. (a) Log–log depth and diameter plot showing Class 2 to Class 5 RECs. Fresh NRECs are also included and span all class types. NRECs dominate below 100 m in diameter and are most commonly similar to Class 4 and 5 craters. Several Class 2 and Class 3 type NRECs are however evident. (b) Log–log plot showing rim height data for Class 2 to Class 5 craters. (c) Linear depth to diameter plot showing fit to the Class 2 distribution. (d) Linear rim height to diameter plot showing fit to the Class 2 distribution

tionship (Fig. 15c, d) over the limited 10 m to 100-m-scale diameter range, consistent with the observations of similar-sized lunar craters (Pike 1977). The linear function of depth (d) versus diameter (D) for our dataset of Class 2 craters (most abundant near pristine class) is $d = 0.082D + 0.31$. For depth versus rim height (r) the function is $r = 0.025D + 0.031$. Note that these relations indicate that Class 2 craters are likely more degraded than fresh bowl shaped craters that typically form with $d = 0.2D$ and $r = 0.04D$ (Pike 1977). The progressive decrease of crater depth and rim height with morphologic class supports our classification scheme and is consistent with the expected degradation of craters with time (e.g. Golombek et al. 2014b; Sweeney et al. 2016). The depth and rim-height data also provide critical information regarding the total amount of degradation between each class. For instance, a single 200 m diameter Class 2 crater in our dataset has a depth of 22 m. Class 5 craters of equivalent diameter have depths ranging from 7 to 11 m. This indicates a total of 11 to 15 m of infill and crater degradation between these two class end members.

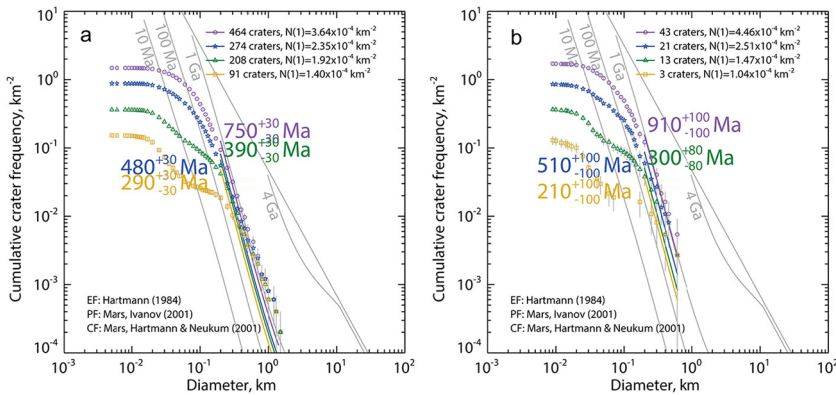


Fig. 16 Cumulative crater size frequency distribution plots for Class 1 to 5 RECs. *Purple circles* indicate Class 1 to 5. *Blue stars* represent Class 1 to 4. *Green triangles* are Class 1 to 3 and *yellow squares* are the Class 1 to 2 craters. **(a)** Plot showing the data for all 44 HiRISE images in all 4 landing ellipses. **(b)** Data from a subset of 3 pairs of HiRISE images in the final landing ellipse E9 that correspond with 3 DEMs

Plotting each classification group (e.g., 1 to 2, 1 to 3) on a cumulative SFD plot provides a timescale for the degradation between each crater class (Fig. 16a). For all RECs >200 m diameter we find a good fit to the isochron indicating an age of 750 ± 30 Ma. When including only those craters in the three DEMs we get a similar, but slightly older age of 910 ± 100 Ma. For Class 1 to 4, 1 to 3 and 1 to 2 RECs >200 m diameter, we find good fits to the isochrons for ages of 480 ± 30 Ma, 390 ± 30 Ma, and 290 ± 30 Ma, respectively, with similar ages for the RECs in the three DEMs (Fig. 16b). These data indicate that a pristine crater degrades to a Class 5 crater in approximately 480 to 750 Ma, with approximately 100 Ma separating each morphologic class.

The plots also illustrate that the observed slope reduction in the SFD at $D < 200$ m occurs even when older classes are not included. The Class 1 to 4 plot for example excludes the most degraded RECs, yet still exhibits a major slope reduction in the data. The roll-off is also present for the Class 1 to 2 craters, although this distribution shows a kink that might indicate multiple crater populations. A steeper portion of the Class 1 to 2 SFD is present from 20 m to 50 m (Fig. 16), which is exactly within the dominant-size range of Corinto REC's. It is possible that not all Corinto secondaries have an obvious bright ejecta blanket and therefore were mistakenly classified as Class 1 or possibly 2. It is also possible that random Zunil secondaries were included in the dataset, although a majority of Zunil's at this range are smaller than the 10-m-scale craters included in this analysis (Preblich et al. 2007).

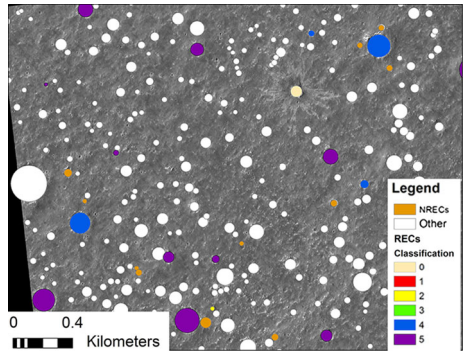
As stated previously, the slope of the SFD for all RECs at $D > 200$ m indicates that they are all $<750 \text{ Ma} \pm 30$ Ma in age. For >200 m diameter craters that are older than 750 Ma, rocks in the ejecta have disappeared. For craters <200 m in diameter, the slope roll-off suggests that, one or all of the following may have occurred: (1) smaller craters have been obliterated through some size-dependent degradation process, (2) smaller craters associated with smaller ejecta block sizes have lost their rocks, also through some size-dependent degradation process, and/or (3) a regolith is preventing rocks from forming. Using the model ages from the class specific SFDs, the maximum age of a Class 2 crater is $290 \text{ Ma} \pm 30$. From the DEM, the total degradation between a 200 m diameter Class 2 and Class 5 crater is 11 m to 15 m. Using a plausible timescale of 450 Ma that separates the maximum age of Class 2 craters from the maximum age of Class 5 craters, we calculate a degradation

rate of 0.02 to 0.03 m Myr⁻¹, which is consistent with erosion rates estimated on Mars over hundreds of Myr timescales (Golombek et al. 2014b). Using depth to diameter scaling relationships from our dataset and these degradation rates, a 100 m Class 2 crater could have been completely obliterated over the 450 Ma timescale. For example, at the higher end degradation rate of 0.03 m Myr⁻¹ it would require only ~270 Ma to completely degrade an 8 m deep, 100 m diameter Class 2 crater. At 0.02 m Myr⁻¹ it would require ~400 Myr. If the depth-dependent crater obliteration rates are reflective of the overall rates of obliteration of ejected rocks and crater rims then surface processes may be responsible for a significant component of the roll-off in the REC SFD, especially at $D < 100$ m.

In terms of rock obliteration, the maximum observed block size in our dataset for 200 m diameter Class 2 craters is approximately 5 m. For 100 m, 50 m, and 10 m-sized craters it is 4 m, 3 m, and 1 m respectively. The similarity of the observed maximum block sizes in Class 2 craters to the modeled maximum block sizes of pristine craters (Melosh 1989) suggests that block obliteration is minimal during the time frame of degradation to Class 2. Based on the SFD of all >200 m diameter Class 1 to 5 craters, it takes >750 Ma to destroy all observable blocks in the ejecta of a 200 m diameter crater. This timescale of obliteration is significantly slower than recent estimates for the preservation timescales of meter-sized lunar rocks by Basilevsky et al. (2013). In their analysis, 99% of all >2 m-sized rocks are removed from a crater over maximum timescales of 150–300 Ma. A comparison of these results to our martian example most likely indicates the importance of micrometeorite bombardment in the breakdown of lunar rocks, a process that does not operate on Mars. Using the SFD-derived timescale for RECs in the Elysium region, a time-averaged degradation rate of ~0.007 m Myr⁻¹ is required to completely degrade a 5 m-sized rock. For a 4 m, 3 m, and 1 m size block the rates are ~0.005 m Myr⁻¹, ~0.004 m Myr⁻¹, and ~0.001 m Myr⁻¹.

The rates of rock obliteration calculated here are an order of magnitude slower than the degradation rates based on infill. This is consistent with results by Golombek et al. (2014b) who suggest that burial by eolian material plays a significant role in modifying the interiors of 10 to 100-m-scale craters while playing less of an important role in modifying their rim or ejecta. Morphometric calculations based on crater infilling may therefore over-estimate the true rate of surface modification of the rocks in ejecta blankets and the rims of craters. Our image-based observations here indicate that the crater interiors are major sediment traps to mobile eolian material (Fig. 12). Sediment trapping must therefore account for a significant portion of the calculated depth-dependent degradation. Eolian materials only remain in the ejecta blankets of the freshest craters temporarily. Starting in the ejecta, the bedforms of a Class 2 crater migrate either away or towards the rim of the crater depending on the seasonal prevailing wind direction (NW-SE, SW-NE) (Reiss and Lorenz 2016). Class 2 and 3 craters exhibit bedforms trapped against the exterior of the elevated rim as well as bedforms on the crater floor (Fig. 12a–d). Eventually, by Class 4 and 5, the majority of the trapped bedforms are gone and the crater shows near complete infill while still maintaining rim relief and preserved ejecta rocks (Fig. 12e–h). This same sequence of infill is observed on the Gusev cratered plains (Golombek et al. 2006a). The Elysium craters indicate that time-averaged burial rates are higher inside of a crater than outside of the crater. We suggest that it is more appropriate to compare rock degradation rates in the ejecta to crater rim degradation rates which are modified under similar surface conditions and are likely composed of similar materials to the ejected blocks. By comparison, the total rim degradation between a Class 2 crater and a Class 5 crater at a diameter of 200 m is at most 6 m. This equates to a maximum rim degradation rate of ~0.01 m Myr⁻¹ over the 450 Myr timescale that separates Class 2 from Class 5. While this rate is sufficient to remove 5 m sized blocks from the ejecta over >450 Ma, this rate is too low to explain the magnitude of the roll-off in the SFD for the

Fig. 17 Example crater count from a HiRISE image showing all counted crater classes, including Class 0 to 5 RECs, similarly fresh NRECs (*orange*), and all other more degraded craters that lack rocks (*white*)



younger morphologic classes. In other words, 5-m-size blocks could not have been completely removed from the ejecta of a 200 m diameter impact crater that is <450 Ma in age. The data also indicate that the total rim degradation between all classes declines with decreasing crater diameter, possibly because their lower rims are less of a topographic obstacle to eolian abrasion and sediment trapping. For 50 m-sized craters that produce ejecta blocks up to 3 m in size (Fig. 11), the total rim degradation from Class 2 to Class 5 is at most 1 m (0.002 m Myr^{-1}), which is an insufficient total amount of degradation to completely obliterate 3 m rocks from the ejecta over the Class 2 to Class 5 timescale. At this crater diameter range, the relief of the crater rim (Fig. 15) is similar to the relief of 1 meter-sized ejecta blocks and offers similar resistance to air flow. The crater rim degradation rates calculated from smaller craters with meter-high crater rims is therefore more reflective of the degradation rates that would have modified meter-sized boulders. We conclude that the magnitude of the slope reduction observed on the SFD plots at $D < 200$ m for all morphologic classes cannot be completely explained by the obliteration of rocks from the ejecta of craters or the destruction of the rim expression of the crater.

3.3 Fresh, Non-rocky Ejecta Craters

If a regolith is buffering and preventing the formation of small RECs, then fresh non-rocky ejecta craters (NRECs) should be abundant across the landing region below the 200 m diameter roll-off threshold in the SFD of the RECs. A portion of the fresh NREC crater count taken across one of the three HiRISE images that correspond with DEMs is shown in Fig. 17. The NRECs are morphologically similar to Class 1 to 5 craters yet lack rocks in their ejecta blanket. The depth to diameter plot in Fig. 15 includes a sample of 176 NRECs. The data confirm the morphologic similarity of the NRECs to the RECs and demonstrate that NRECs are most abundant at diameters <200 m. The largest NREC in the three HiRISE images is 180 m which corresponds to the <200 m roll-off on the REC plot. Like the REC dataset, the bulk of the NRECs can be classified as Class 4 and 5 craters although several NRECs are morphologically similar to Class 2 and 3 craters.

Here we compare the cumulative and incremental size frequency distribution histogram of the RECs to the histogram that includes both the RECs and the NRECs together (Fig. 18). The data here is only derived from the three images that correspond with the three HiRISE DEMs. We also provide a crater count from one of the HiRISE images that includes all craters for comparison, regardless of the preservation state and presence or absence of rocks. Importantly, the inclusion of NRECs significantly increases the slope of the distribution above that of the REC only plot for craters <200 m in diameter. While the slope of the

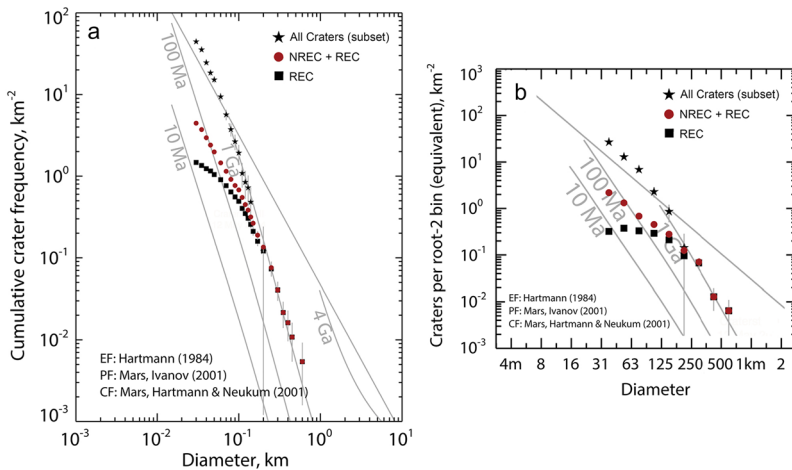


Fig. 18 Cumulative (a) and incremental (b) plots comparing the slopes of the REC, NREC+REC, and all craters size frequency distributions. These data were derived from the three HiRISE images that correspond with DEMs in the final landing ellipse E9. The slope of the REC plot rolls-off (decreases) at $D < 200$ m while the slope of the NREC+REC dataset follows the equilibrium slope (-2) at that same diameter range. This indicates that some component of the REC roll-off is due to crater obliteration. However, obliteration cannot account for all of the roll-off. A comparison of the crater frequency between the REC only plot and the NREC+REC plot provides an estimate of the total area covered by regolith. See Table 2 for more data

distribution steadily declines with decreasing diameter for the REC plot (in a manner similar to the bulk dataset), the slope of the NREC + REC cumulative frequency plot stabilizes near -1.8 , which is a similar slope to the Hartmann (1984) equilibrium function. This near-constant slope of the NREC+REC cumulative function at smaller diameters implies that size-dependent degradational surface processes are important here. In other words, smaller craters (and likely the rocks associated with them) are degrading at a faster rate as compared to larger craters. However, this degradation cannot account in total for the more significant roll-off that is observed at small diameters on the REC-only plot. We therefore suggest that the REC roll-off is partially a function of a regolith that is preventing smaller rocky craters from forming.

Using the Melosh (1989) maximum depth of excavation relationship and the ~ 200 m cut-off diameter, we suggest an approximate maximum regolith depth in southwestern Elysium Planitia of 17 m. Other excavation models (Hermalyn and Schultz 2011; Grieve et al. 1981; Stoffer et al. 1975) provide a maximum regolith depth range of 12 m to 18 m. Because these relationships assume a steep impact, it is possible that some craters excavated rocks from shallower depths (Schultz and Anderson 1996). We therefore treat these constraints as representatives of the thickest possible regolith at southwestern Elysium Planitia. Importantly, the data indicate that there are multiple RECs below this diameter, suggesting that the regolith is possibly slightly thinner throughout the study region. To better estimate the thickness of the regolith, we compare the frequency of craters (number of craters area^{-1}) at each diameter bin below 200 m on the REC plot (subset in DEMs) to the crater frequency on the NREC+REC plot (Fig. 18). A comparison of the crater frequency between the two plots accounts for crater degradation (indicated by the near equilibrium slope of the NREC+REC plot) and therefore reveals the number of rocky craters per area that were prevented from forming by the presence of a regolith. For example, using the incremental plot of the subset dataset (Fig. 18) there are 213 NREC + REC craters in the 63–87 m (root 2 binning,

Table 2 Comparison of the number (n) of RECs ($n1$) and NRECs+RECs ($n2$) over the same subset area (3 HiRISE images) in each root-2 bin. Crater counting error is derived from Poisson statistics (\sqrt{n}). Data includes an evaluation of the % area covered by regolith, derived from a comparison of the crater frequencies of these two crater groups (see methods). Data relevant to the target HP³ penetration depth (3 to 5 m) is highlighted

Diameter Bin (m)	Depth (m) (Melosh 1989)	Depth (m) (Hermalyn and Schultz 2011)	Depth (m) (Grieve et al. 1981)	$n1 = \text{RECs}$	Error $+/- n1$	$n2 = \text{NRECs} + \text{RECs}$	Error $+/- n2$	$n1/n2$	Percent area with Regolith Thickness > Excavation Depth	% Area $+/-$ Error
31	3	2	3	100	10	682	26	0.15	85	+2/-2
44	4	3	4	117	11	411	20	0.28	72	+4/-4
63	5	4	6	103	10	213	15	0.48	52	+8/-9
88	7	5	8	91	10	141	12	0.65	35	+11/-13
125	11	8	11	66	8	87	9	0.76	24	+16/-20
177	15	11	16	30	5	39	6	0.77	23	+23/-23
250	21	15	23	21	5	22	5	0.95	5	+34/-5
354	30	21	32	4	2	4	2	1.00	0	+67/-0
500	42	30	45	2	1	2	1	1.00	0	+83/-0

Hartmann 2005). Craters of this size excavate material into their continuous ejecta from a maximum depth of approximately 4 m to 8 m using the various excavation relationships. In that same bin, there are only 103 RECs. This indicates that 52% (error +8% / -9%) of all relatively fresh, Class 1 to 5 impact craters of this size lack rocks in their ejecta blanket, or did not access the rock-producing unit. In other words, 52% of this sample set area has a regolith that is at least 5 m to 7 m thick, assuming the Melosh excavation relationship, which represents a plausible median range of all excavation depth relationships. Table 2 highlights the crater data at each root-2 incremental bin with the estimated excavation depth using different excavation relationships. The data suggests that the largest disparity between the number of RECs and the NREC+RECs per km² occurs within the 31 m to 43 m diameter bin. For this size range, 85% (error +2% / -2%) of all mapped craters lack rocks in their ejecta. This indicates that the region has a regolith that is at least 3 m thick over that coverage area using the Melosh (1989) excavation relationship. Using the low end member and high member excavation relationships, this diameter bin implies regolith at least 2 m to 4 m thick.

3.4 Crater Morphology and Regolith Thickness

Each HiRISE image in the InSight landing region was scanned for evidence of concentric craters that indicate a material strength transition at depth (Quaide and Oberbeck 1968; Senft and Stewart 2007; Bart et al. 2011; Bart 2014). Concentric craters exhibit an exterior crater with a typical bowl-shaped interior wall and elevated crater rim. The floors of these craters contain a second, smaller crater that is entirely concentric to the exterior crater rim. This smaller nested crater marks the depth transition into a more competent unit and serves our study as an independent method for estimating regolith thickness. Flat-floored or mounded craters, which are representative of smaller impact events that did not excavate the more competent material, are difficult to distinguish from craters that have been infilled. We therefore present regolith thickness estimates using the morphometric properties of only concentric craters.

The mapping analysis across the InSight region revealed dozens of concentric craters, providing independent evidence for a material strength transition that is consistent with regolith over more competent material. Figure 19 shows representatives of the morphologic range of these craters. They are strikingly similar to lunar mare concentric craters, both in scale and morphology (Oberbeck and Quaide 1967; Quaide and Oberbeck 1968; Bart et al. 2011). Here, we describe the morphometry of 32 examples of Class 0 to 2 concentric craters which represent the youngest, most morphologically pristine craters in our dataset. The concentric crater dataset includes mostly rocky ejecta craters. However, a minority of young non-rocky craters also show the nested crater morphology. We analyzed the youngest crater classes to avoid the effects of crater infilling, which partially or completely masks the inner crater. More heavily modified Class 3 to 5 concentric craters however were also identified (Fig. 19h, i). The range of diameters in the concentric crater sample set is 17 m to 96 m with a mean and median of 41 m and 47 m, respectively. Importantly, the smaller interior craters in all examples exhibit clearly defined rocky margins. This supports the hypothesis that a rock-producing unit is causing the material strength transition at depth. For the more degraded Class 3 to 5 craters, rocky margins within an inner crater can be seen in some rare cases where the interior is exposed (Fig. 19h, i).

Using the measured interior and exterior diameters of the concentric craters and the constant k of 0.86 from Quaide and Oberbeck (1968) we provide regolith thickness estimates for the Class 0 to 2 examples using Eq. (1) (Table 3). The D_F/D_A values for all craters occur within the range of 0.2–0.7 (Bart 2014). The k constant, which is the ratio of the exterior crater diameter (D_T) as it is measured at the level of the ground to the apparent crater

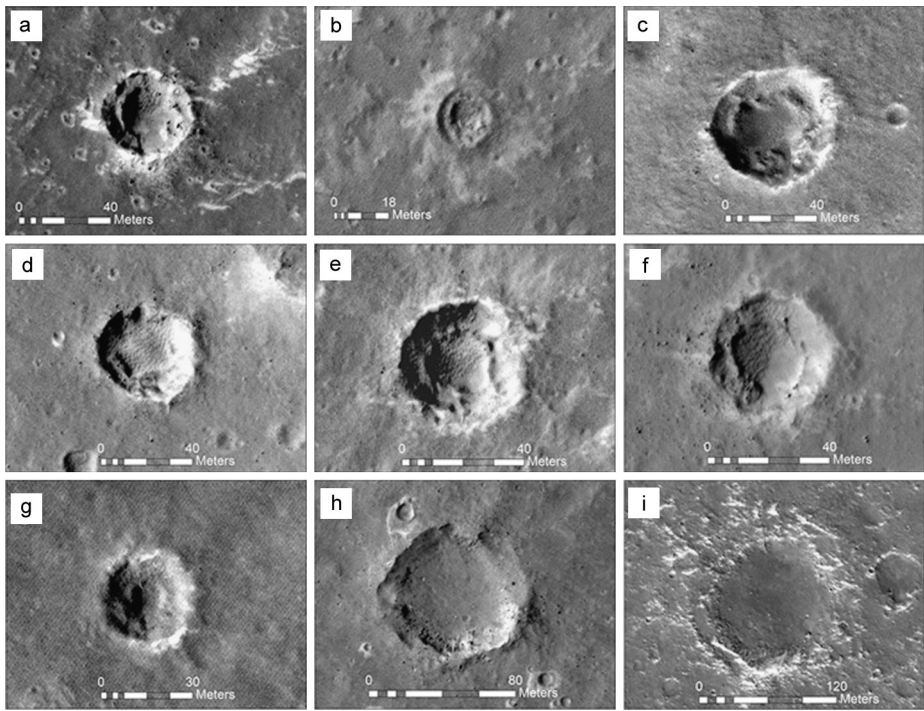


Fig. 19 Examples of concentric or nested craters in the InSight landing region in various states of degradation in HiRISE images. Plates (a)–(g) represent Class 0 to 2 concentric craters. Plates (h) and (i) represent degraded concentric craters, showing inner craters that are marked by a more resistant, rocky unit. Image (h) represents a Class 4 crater. Image (i) is too degraded to be classified as a REC yet still shows an inner ring that is associated with a rockier unit

diameter (D_A) as it is measured from rim to rim, was derived experimentally by Quaide and Oberbeck (1968) to best match lunar surface properties. However, its applicability to Mars is uncertain. We conducted a sensitivity analysis of the k constant by measuring D_T and D_A using the HiRISE DEMs. This allowed us to more accurately measure D_T from a ground level, determined by fitting a plane across the width of the crater at the elevation of the surrounding terrain. While our results indicate that 0.86 is reasonable as a mean value for k , the extremes of possible measured values include 0.7 and 1.0, although a 1 to 1 ratio of D_T to D_A is extremely rare and does not conform to the typical bowl-shaped morphology of simple craters. This range results in a factor of 1 to 4 uncertainty in regolith depth where smaller values of k result in a thinner estimated regolith thickness and larger values of k (however unlikely) result in a thicker estimate. Although larger Class 0 craters (Corinto secondaries) that show concentric craterforms are rare, a preliminary analysis of their ground level and apparent diameters reveals a slightly lower ratio range between 0.7 and 0.8. A likely angle of repose of 30° for sand-sized materials is used, although crater interior slope data for Class 1 to 2 craters indicate a possible range from 25° to 35° . Furthermore, where rocky outcrops are observed, slopes can exceed 35° . A 10° variation in angle of repose results in a factor of 1.4 difference in the regolith thickness estimates.

The data using the Quaide and Oberbeck (1968) model (Eq. (1)) indicate a range in the regolith thickness estimates between 1.6 m and 7.7 m with a mean of 4.3 m and a median of 4.1 m (Table 3). Importantly, the values are entirely consistent with the REC size frequency

Table 3 Morphometric data of sample of concentric, nested craters, including an analysis of the regolith thickness using equation (1)

Crater ID	Figure	Apparent diameter, D_A (m)	Inner diameter, D_F (m)	DA/DF	Regolith thickness, t $k = 0.86$ (m)	Regolith thickness, t $k = 1.0$ (m)	Regolith thickness, t $k = 0.70$ (m)
7592		17	8	0.46	1.9	2.6	1.2
8173		24	15	0.63	1.6	2.6	0.5
2416		25	16	0.64	1.6	2.6	0.4
6836		26	15	0.58	2.1	3.2	0.9
6728		26	13	0.50	2.7	3.8	1.5
3671		31	13	0.42	4.0	5.2	2.5
6257	19g	31	12	0.39	4.3	5.5	2.8
6628		32	12	0.38	4.5	5.8	3.0
6365		33	19	0.58	2.7	4.1	1.2
6245		33	15	0.45	3.9	5.2	2.3
9907		34	18	0.53	3.3	4.6	1.7
6390		36	17	0.47	4.0	5.5	2.4
6409		36	19	0.53	3.5	4.9	1.8
1670		37	24	0.65	2.3	3.8	0.6
8803	19a	38	22	0.58	3.1	4.6	1.3
6186	19f	41	21	0.51	4.1	5.8	2.2
5114		41	17	0.41	5.3	7.0	3.4
5023		43	14	0.33	6.7	8.4	4.7
9906	19e	44	21	0.48	4.9	6.7	2.8
6937		45	28	0.62	3.1	4.9	1.0
5315		45	22	0.49	4.8	6.7	2.8
6766		46	27	0.59	3.6	5.5	1.5
10		48	28	0.58	3.9	5.8	1.6
8894	19c	52	30	0.58	4.3	6.4	1.9
5135		64	33	0.52	6.4	9.0	3.4
5288		66	31	0.47	7.5	10.2	4.4
5958		72	39	0.54	6.6	9.6	3.3
8652		74	37	0.50	7.7	10.7	4.3
2075		87	55	0.63	5.7	9.3	1.7
7637		92	60	0.65	5.5	9.3	1.3
6737		93	65	0.70	4.3	8.1	0.0
5110		96	57	0.59	7.4	11.3	3.0
Mean					4.3	6.2	2.1
Median					4.1	5.7	1.8

distribution data presented in the previous sections across the full range of models for depth of excavation. Using a k constant of 1.0, the mean and median regolith thickness values are 6.1 m and 5.7 m, respectively. Using a k value of 0.7 results in a much lower mean regolith thickness of 2.1 m and median of 1.8 m.

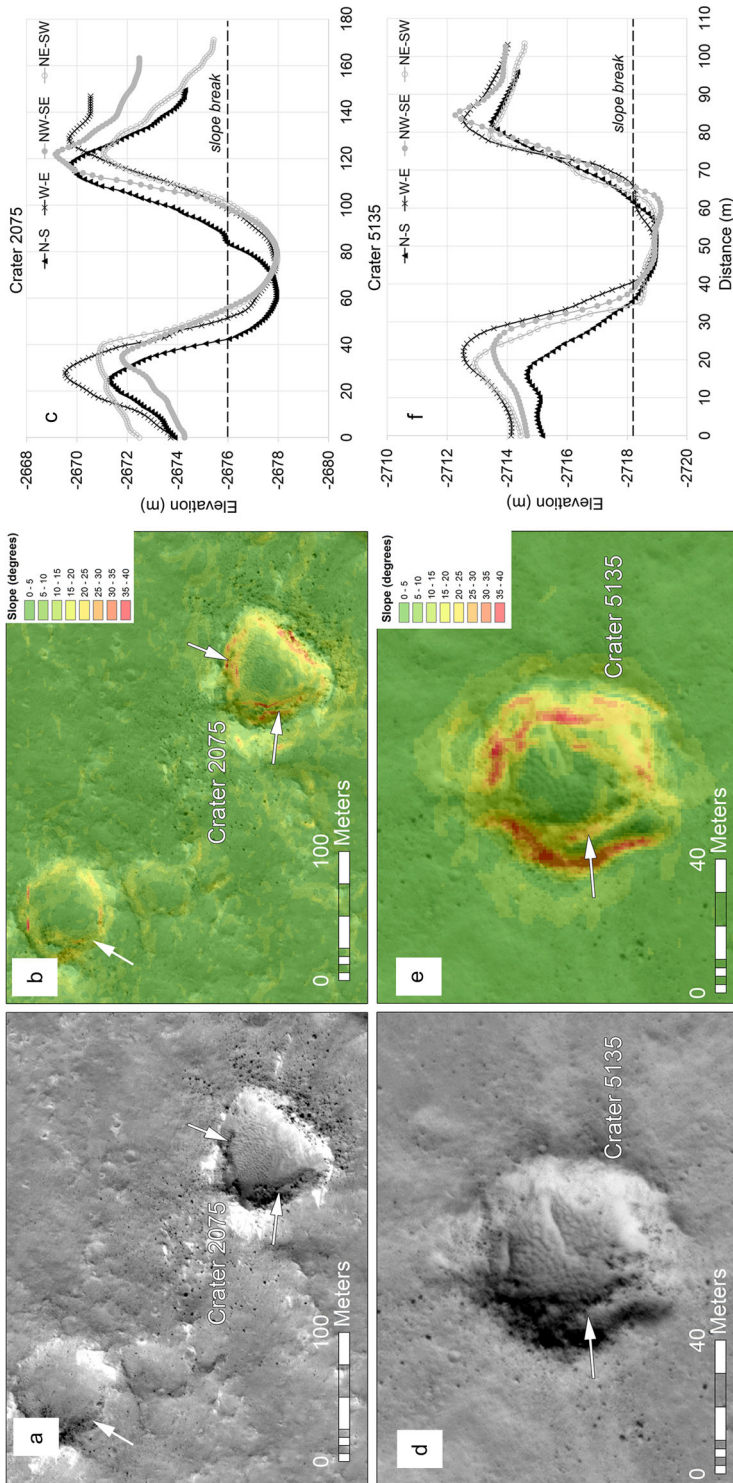


Fig. 20 HiRISE images and topography data of concentric craters showing slope transitions at depth (white arrows). (a) orthoimage of crater 2075. (b) HiRISE DEM, 1 m slope map showing steep slopes that correspond with the appearance of a blocky unit within the crater. (c) HiRISE DEM topographic profiles collected across the crater showing minor slope inflections that correspond with the location of the more resistant inner crater. Plates (d), (e), and (f) show similar data for crater 5135. The morphometric data confirm the likelihood of a meters thick regolith that rests on top of a more resistant rocky unit

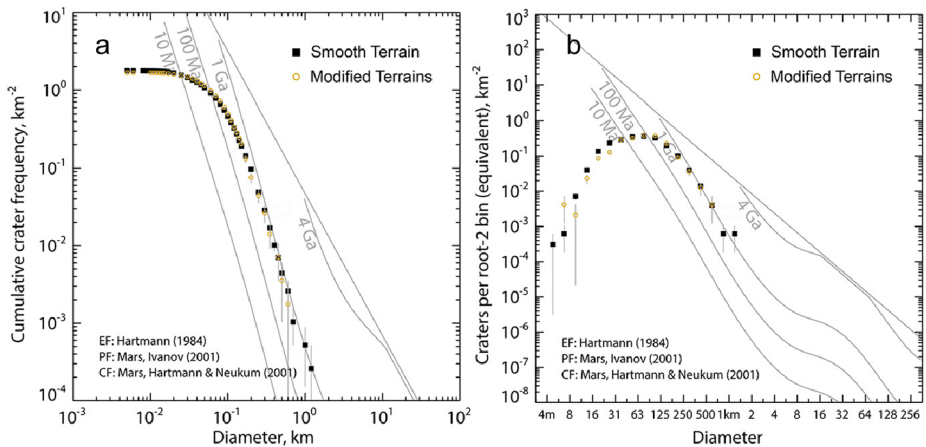


Fig. 21 (a) Cumulative and (b) incremental crater size frequency distribution plots comparing the distribution of RECs on Smooth Terrain versus the more modified terrain types of Etched, Gradational, and Dark. The data show similar slopes, however the noticeably lower slope of the modified terrain distribution at $D < 50$ m is likely related to obliteration of the smaller RECs here, either by erosion or burial

Topographic profiles were also taken across the concentric craters from the HiRISE DEMs to compare to the empirical model. Unfortunately, most concentric craters are too small and the interior walls are spanned by only a handful of DEM (1 m) postings. Some profiles however show minor slope inflections that correspond with the observed inner crater (Fig. 20). Slope maps also reveal evidence for slope changes along the interior that correlate with the occurrence of an inner crater. In many instances, the interior slope of the inner crater is steeper than the interior slope of the outer crater suggesting a change from a less competent upper unit to a more resistant lower unit. Crater 2075 (ID number derived from ArcGIS shapefile database) exhibits an obvious slope change at a depth of 5 to 6 m, measured vertically from the top of the crater rim (Fig. 20a, b, c). Measured from the surrounding plains, the depth to the slope break is 2 to 5 m depending on the elevation that is used to define the plains. Using the Quaide and Oberbeck (1968) model, the estimated regolith thickness is 5.7 m using $k = 0.86$, 9.3 m for $k = 1.0$, and 1.7 m for $k = 0.7$. Crater 5135 is another type concentric crater that shows a slope inflection in all profiles at a depth of 3 to 5 m measured from the rim and 2 to 4 m from the surrounding plains (Fig. 21d, e, f). For comparison, the modeled regolith thickness of this crater is 6.4 m for $k = 0.86$, 9.0 m for $k = 1.0$, and 3.4 m for $k = 0.7$. The topographic profiles suggest that the competent unit is at a depth that is consistent with the model-based prediction of regolith thickness for both craters (Eq. (1)), specifically for k values between 0.7 and 0.86. However, for other example concentric craters including Crater 6186 and 5114 in our database the modeled regolith thickness exceeds the measured depth of the crater. Crater 6186 for example is ~ 3 m deep, yet the model-based regolith thickness is 4.1 m at $k = 0.86$. Furthermore, the observed inflection in the slope on the topographic profiles occurs at a much shallower depth of 1.0 m to 2.5 m. A better match between the observations and the model in this case occurs when the k constant is adjusted to lower values, however, other sources of uncertainty may be responsible, including the depth of eolian infill, impact angle and target properties (Quaide and Oberbeck 1968). Crater 6186 and 5114 are both ~ 40 m in diameter, which falls within the dominant diameter range of rocky ejecta Corinto secondaries. A lower impact angle and different k constant relative to primaries might play a role in the deviation between observation and the model.

3.5 Regolith Thickness Variability

The previous sections demonstrate that a meters-thick regolith exists across the InSight landing region. However, it is unclear whether this regolith is continuous in thickness across the final landing site and the broader area. Terrain mapping (Golombek et al. 2016b, [this issue](#)) revealed a variety of landform morphologies that suggest an overlying smoother unit (Smooth Terrain) has been partially stripped to create a more etched landscape (Etched, Gradational, and Dark terrains). We posit that this smoother unit represents a region with a fully intact regolith, while the more modified terrains represent regions where the regolith has been partially removed. Here, we isolate the SFD data of the RECs on the Smooth Terrain from the REC dataset that corresponds with the Etched, Gradational and Dark terrain types to test this hypothesis (Fig. 21). We combined the data from these more modified terrains onto one SFD plot due to their limited areal coverage and low number statistics. We compare the cut-off diameters at which the SFD rolls over between the different terrain datasets.

The slope of the SFD on both curves (Fig. 21) is similar over most diameter bins and almost identical for diameters >200 m. However, at $D < 50$ m there are more RECs on the Smooth Terrain per area relative to the modified surfaces. Surface modification associated with the formation of Etched, Gradational, and Dark Terrains may have played a role in removing or burying the smaller RECs. Meter-scale bedforms in the Etched Terrain for example could easily mask small rocks. Furthermore, the overall rock abundance is much higher in the Etched Terrain than in the Smooth Terrain (Golombek et al. 2016b, [this issue](#)). This makes it difficult to definitively identify a uniquely rocky ejecta blanket for smaller craters on the Etched Terrain.

To more broadly capture regolith thickness variations across the region we generated a density map of the RECs using the kernel density tool in ArcGIS. The kernel density analysis reveals that there are regions of higher REC density at locations that are independent of terrain boundaries. In other words, there is no obvious correlation, above the scatter of the density data, between terrain type and REC density. In a map that includes all RECs (Class 0 to 5), the highest density occurs in the northern-most ellipses (E9, E17) within the Smooth Terrain (Fig. 22a). Density variations are also evident in other ellipses. Removing the Class 0 Corinto secondaries from the dataset illustrates that some but not all of these higher density locations are associated with dense secondary crater chains (Fig. 22b). These chains are easily identifiable in THEMIS nighttime IR imagery as dark, low thermal inertia, north-south trending streaks (Fig. 23). The point data were also divided by crater diameter to identify diameter-dependent density trends. The data indicate that even when Class 0 craters are excluded, the variations in the data are largely caused by craters between 20 m and 60 m in diameter (Figs. 22c, d, e). The high-density concentrations largely disappear above 100 m. This range is entirely consistent with the dominant size of Corinto secondaries and may be reflective of contamination in our dataset where the Corinto craters were included as Class 1 or 2 craters. The size range is however too large to be related to distal Zunil secondaries (McEwen et al. 2005; Preblich et al. 2007). We used the characteristically bright, lobate ejecta patterns to identify Class 0 Corinto secondaries. It is possible that not all Corinto secondary craters are associated with this pattern. However, the high-density concentrations are still evident in E9 and E17 when fresh, Class 1, 2, and even 3 craters are removed from the dataset (Fig. 22f). Because Class 4 and 5 craters are significantly more degraded than the young Corinto secondaries, it is unlikely that the higher density of these craters can be attributed to their contamination. Rather, the higher density could be attributed to a locally thin regolith. The highest density zone in E9 and E17 in all cases is spatially correlated to a north-south trending wrinkle ridge (Fig. 24).

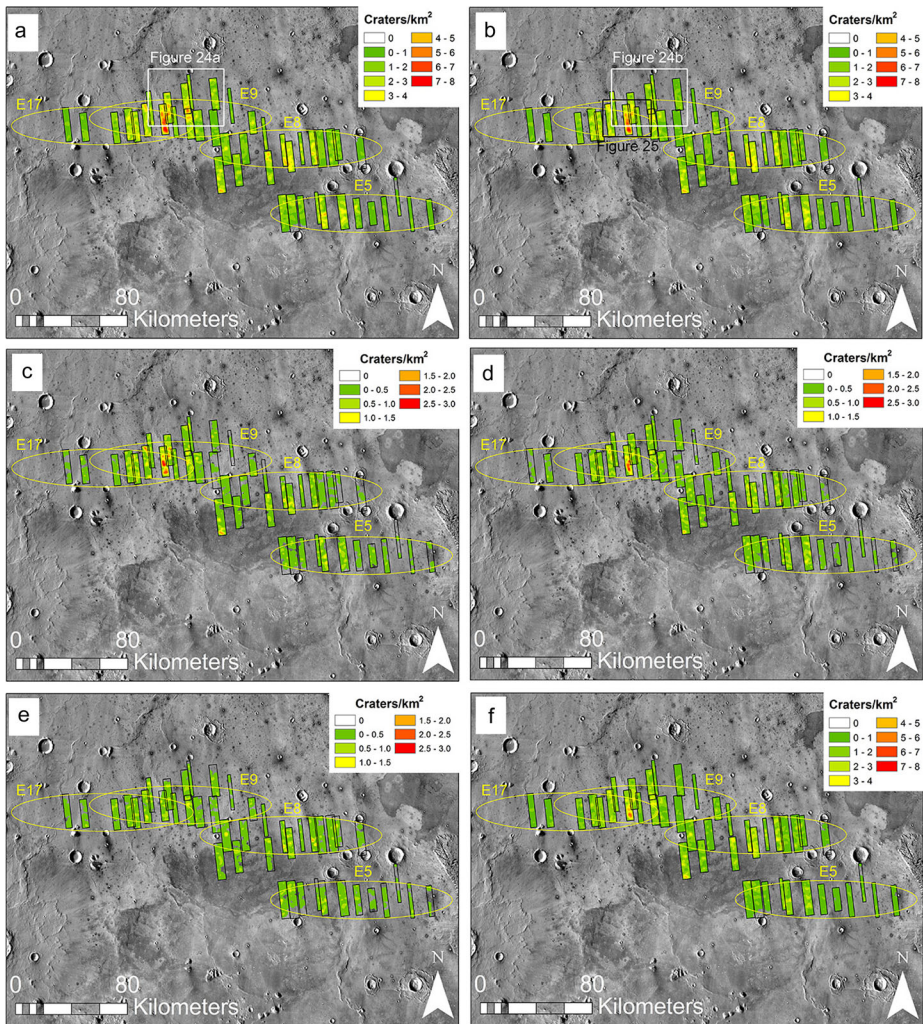


Fig. 22 ArcMap kernel density maps showing the density distribution of RECs across the final 4 landing ellipses. **(a)** Density map of all Class 0 to Class 5 craters. **(b)** Map excludes Class 0 craters. **(c)** Density of all 20 m to 40 m diameter RECs, excluding Class 0. **(d)** Density of all 40 m to 60 m diameter RECs, excluding Class 0. **(e)** Density of all 60 m to 80 m diameter RECs, excluding Class 0. **(f)** Data for only the Class 4 and 5 RECs, including all sizes. These maps suggest that not all high density regions are associated with known Corinto crater secondaries. They also demonstrate that the higher density locations are predominantly associated with craters <60 m in diameter but are not exclusive to only the freshest small craters.

4 Discussion

4.1 Near Surface Stratigraphy at Southwestern Elysium Planitia

The SFD and crater morphology methods both independently confirm the presence of a meters-thick regolith across the InSight landing region in southwestern Elysium Planitia. However, the detailed stratigraphy of the regolith and the rock-producing unit at depth remains uncertain. The material strength, internal structure, thickness, and lateral continuity

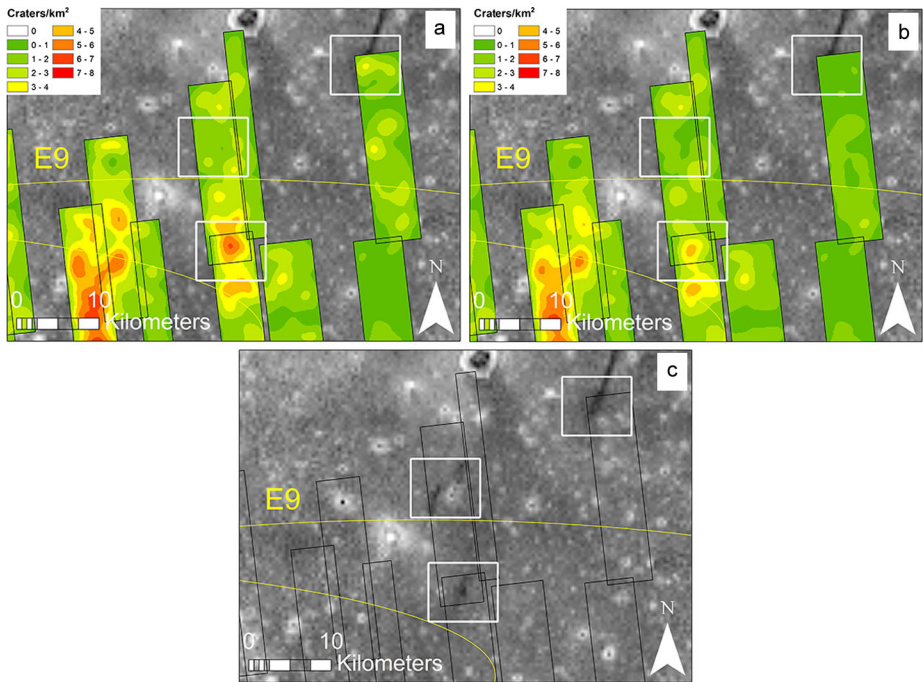
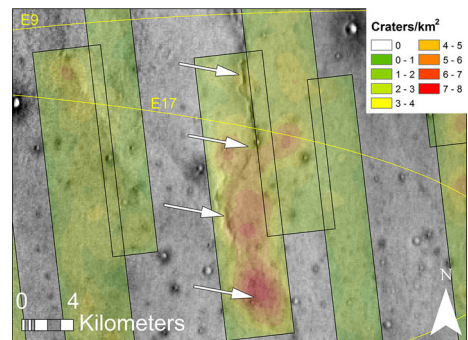


Fig. 23 Kernel density maps over the northern portion of ellipse E9 overlain on the THEMIS nighttime mosaic. **(a)** Density map of all RECs including Class 0 to Class 5 craters. **(b)** Density map of only Class 1 to Class 5 RECs. Subtraction of the Class 0 RECs from the dataset removes some of the higher density locations. The higher density locations that were removed closely correspond with NE-SW trending Corinto secondary rays that show up in THEMIS nighttime images as dark streaks **(c)**. However, removing the Class 0 craters from the dataset did not remove all of these higher density locations. A high density region persists in the west-central region of E9

Fig. 24 Kernel density map overlain on the THEMIS daytime IR mosaic showing the correlation between a higher density REC location and a north-south trending wrinkle ridge (*white arrows*). The wrinkle ridge appears to have a locally thin regolith near the center of the E9 ellipse



of both units could be variable. The SFD plots, crater morphology, and density maps for example hint at heterogeneity in the depth to the rock-producing unit. Furthermore, not every REC of equal class shows an identical rock abundance. HiRISE images reveal that any 200 m to 1.4 km diameter Class 2 REC exhibits a relatively high rock abundance in its ejecta, with a maximum cumulative fractional area (CFA) of rocks of $>30\%$ nearest to the crater rims (Golombek et al. 2016b, [this issue](#)). Furthermore, the rocks extend outward from the rim by

approximately one crater diameter, forming a continuous annulus of rocky ejecta (Fig. 7a, b). However, smaller Class 2 RECs, specifically in the range of 30 to 50 m often exhibit only a handful of ejected rocks that are discontinuously distributed (Fig. 10). The maximum CFA of rocks surrounding a 50 m Class 2 crater for example is only $\sim 10\%$ near the crater rim. This includes the nested craters (Fig. 19). The meter-sized blocks that are present in the ejecta of concentric craters suggest that these events had sufficient energy to disaggregate the strong lower target and lift large blocks beyond the crater rim. However, the low rock abundance associated with many of the freshest concentric craters might suggest that the target strength transition is not associated with a continuous, competent, rock-producing layer at depth. In fact, some concentric craters completely lack rocks in their ejecta. It is therefore possible that the smaller impact events are re-working only a few isolated boulders that occur within the column of finer regolith. The SFD plot from the entire dataset indicates that there are few <30 m diameter rocky craters. This suggests that craters of this size only excavated an upper, finer-grained regolith, while craters in the concentric crater size range (mean of 41 m) excavate some rocks from a slightly deeper depth. Furthermore, from 30 m to 200 m in diameter, the proportion of RECs relative to NRECs increases (Fig. 18) as the continuity of rocks in the ejecta blankets of the RECs increases. These observations suggest a vertical stratigraphy that is represented by an increase in rock abundance and material strength with depth.

To aid in our subsurface interpretations we searched the Elysium region for vertical exposures in terrains of similar surface morphology (e.g. lava plains) and age (Early Amazonian to Hesperian). Located ~ 900 km to the northwest of the InSight landing region, Hephaestus Fossae provides a ~ 650 -km long continuous exposure of Hesperian-age strata (Fig. 2 for regional context). Hephaestus Fossae is a fracture system that extends radially off the western edge of the Elysium volcanic rise with a regional northwest strike. Several orthogonal fracture sets within the larger northwest trending fracture system expose a three dimensional view of the shallow subsurface. The fracture exposes Late Hesperian-age strata along its entire length, crossing a contact between the Late Hesperian Transition unit (IHT) at the system's southeastern end and the Late Hesperian Lowland unit (IHL) at its northwestern end (Tanaka et al. 2014). HiRISE imagery over Hephaestus Fossae reveals three distinct units in the shallow subsurface that include, from stratigraphically lowest to highest: (1) a massive, strong fractured unit, (2) a coarse boulder-rich brecciated unit, and (3) a finer-grained, largely boulder-free (at the resolution limit of HiRISE) upper unit (Fig. 25).

The fracture spacing and orientation of the lower most massive unit are similar to orthogonal to hexagonal columnar joints in thick basaltic lavas. The unit outcrops in what appears to be a steep sloped escarpment, with talus below. The steep slope suggests a strong, coherent unit that is steeper than the angle of repose, with talus on the slope below at the angle of repose. The lack of bedding at HiRISE resolution within this unit and its steep, vertically-jointed outcrop suggests igneous rock. The presence of basaltic lava within the shallow stratigraphy of the northern plains is consistent with findings by Catling et al. (2011, 2012), who interpreted the presence of large, competent boulders in the ejecta of northern plains craters as evidence for shallow lava flows. Impact craters on the terrain surrounding Hephaestus Fossae also exhibit boulder-sized rocks in their ejecta. Immediately on top of the massive unit, we observe a thin, coarse brecciated unit that contains meter to ten-meter scale boulders. This unit fines upwards into the uppermost finer-grained unit and shows a hint of stratification at the resolution limit of HiRISE (Fig. 25c). The uppermost unit shows no obvious bedding or interior stratigraphy, although the occasional lower-albedo, boulder-sized rock is observed within or on the exposure. It is not clear whether these rocks are perched on the slope of the unit, representing surface rocks that rolled off onto the exposure as the slope

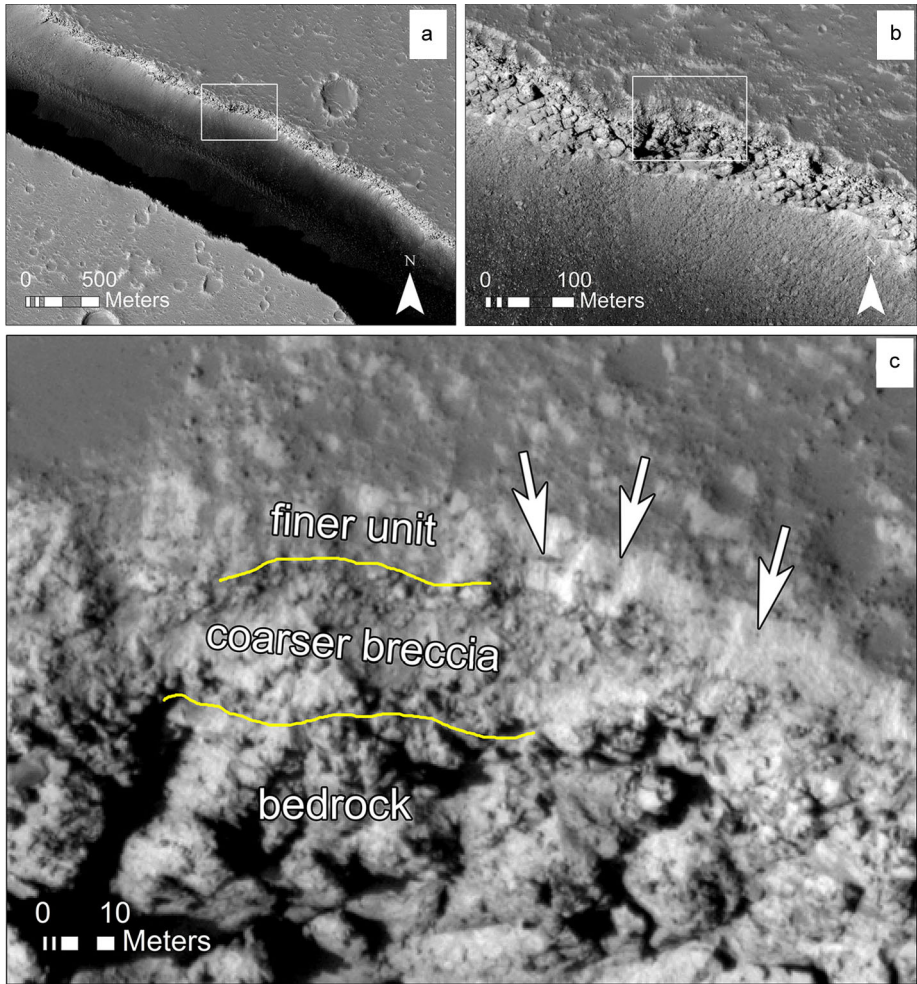


Fig. 25 HiRISE image PSP_002359_2020 over a portion of Hephaestus Fossae. **(a)** Zoomed-out context of the fracture and the inset region of **(b)**. **(b)** Zoomed-in view of laterally-continuous, horizontally-stratified material exposed along the south-facing wall of Hephaestus Fossae. Note the steep exposure of a fractured bedrock unit and the talus below (*lower half of image*), which is likely at the angle of repose. **(c)** Zoomed-in view of the upper 20 to 30 m of the exposure. The more competent, fractured bedrock unit is overlain by brecciated material. This brecciated unit is coarser than the overlying unit. The overlying finer material generally lacks evidence for boulders above the resolution limit of HiRISE. However, some boulder-sized clasts and possible coarser horizons are visible within the upper unit (*arrows*). It is unclear whether these coarser materials have rolled down the slope onto the exposure of the finer unit, or whether they are contained within the unit. The rock abundance of these boulders in/on the finer unit is similar to the overlying flat terrain. We interpret the brecciated unit and finer-grained unit as a stratified, fining upwards sequence of regolith that rests on top of competent bedrock (likely a lava flow)

back-wasted, or are wholly contained within the stratigraphy of the finer material. The latter interpretation would suggest that boulders are present, however at a very low abundance, within the stratigraphic column of the upper unit. The low rock abundance in the exposed section of the fine-grained unit is consistent with the overall low rock abundance on the nearby, relatively smooth cratered plains surface.

We interpret the transition from the massive basal unit to the uppermost finer-grained unit along the Hephaestus exposure as a transition from bedrock to regolith. The brecciated unit may be indicative of a lava flow or other competent bedrock body that was broken into boulder-sized clasts through impact gardening. The fining upwards structure suggests an increase in fracture density that is likely due to size-dependent penetration of progressively smaller, but larger number of impacts as would be expected for an impact generated regolith (Hartmann 1973; Hartmann et al. 2001). The measured width of the fine-grained unit along the south-facing exposure in Fig. 25 is 8 to 15 m. Assuming that the slope of the finer unit is close to the angle of repose for sand to gravel-sized material ($\sim 30^\circ\text{--}40^\circ$), and because the emission angle of HiRISE is roughly normal to this exposure, we estimate a thickness of 4 m to 10 m for the fine-grained unit using trigonometric relationships (no HiRISE stereopairs at time of observation). Our evaluation of all HiRISE images across the Hephaestus fracture system reveals that this stratigraphy is laterally continuous in structure and thickness in all compass directions for hundreds of kilometers, regardless of the strike of the outcrop or look angle of the camera. This is consistent with both a flood lava flow hypothesis for the competent bedrock unit and a regolith hypothesis for the uppermost unit.

The Hephaestus exposure represents the type example of our proposed stratigraphy beneath the InSight landing site. The vertical variations in the stratigraphy that are visible in the exposure are consistent with the observations of Etched and Smooth Terrain, the roll-over diameters on the SFD plots, the morphology and rock abundance of the ejecta blankets, and the presence of concentric, nested craters. These observations also suggest that while many <200 m-sized RECs have rocks in their ejecta blankets, many smaller craters may have excavated a deeper, coarser unit of the regolith that contains loose, boulder-sized rocks, as opposed to a fully intact bedrock layer. The higher rock abundance in the topographically lower Etched Terrain may therefore be related to the exposure of this coarser, boulder-rich unit by eolian deflation, which must have occurred relatively recently (Fig. 5b). The target strength transition that is indicated by the concentric craters may be due to the transition from the finer-grained surface material (material that can be moved by the wind) to the boulder-rich, brecciated unit rather than a transition from weak regolith to intact, hard bedrock. Our estimates of regolith thickness that compare the SFD of rocky and non-rocky craters in Sect. 3.3 may therefore be more representative of only the finest, upper portion of the regolith that lacks rocks that are larger than the resolution limit of HiRISE.

4.2 Regolith Production Rates for Hesperian to Amazonian Mars

Our data suggest that the finest-grained portion of the regolith is almost everywhere \geq approximately 2 m to 4 m thick across the InSight landing region. However, the data also indicate that not all 100 m to 200 m diameter craters accessed a rock-producing unit. Furthermore, the rocky materials excavated by <200 m sized craters may actually be derived from a coarser-grained column of brecciated regolith. Therefore, a reasonable maximum regolith thickness that includes even the coarser-grained fraction and that assumes steep impact and excavation is 12 to 18 m. The full range of possible regolith thickness values for the Hesperian-age terrain here is consistent with the 3 m to 14 m estimate for Early Amazonian to Late Hesperian age terrains by Hartmann et al. (2001) based on expected regolith production from the cratering rate. Crater statistics from Tanaka et al. (2014) using all craters >5 km in diameter suggest an Early Hesperian age (eHT) for the general region. To better constrain regolith production rates we independently evaluated the age of the specific terrain at the landing site from crater statistics using two different areas and minimum diameters. First, we counted all craters that are

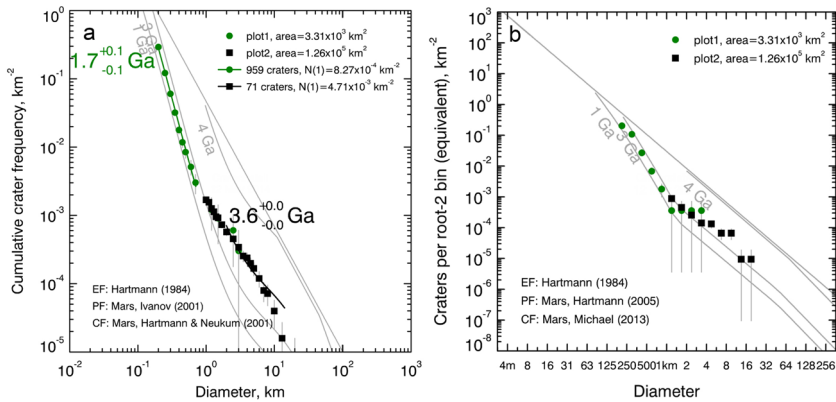


Fig. 26 (a) Cumulative size frequency distribution plot showing two crater counts over the InSight landing region. A regional count (*black squares*), derived from craters >2 km in diameter reveals an Early Hesperian model age that is consistent with the regional geologic mapping of Tanaka et al. (2014). A more localized count (*green circles*) on the Smooth Terrain, derived from craters >200 m and <1 km in diameter over a smaller area suggests a younger surface age in the Early Amazonian. (b) Incremental version with root-2 binning

>200 m in diameter on 3,310 km² of the Smooth Terrain using a CTX mosaic. Second, we counted all craters >1 km in diameter across a 126,000 km² of eHt using the THEMIS daytime IR mosaic. The data confirm an Early Hesperian model age of 3.6 Ga for $D > 2$ km (Fig. 26). However, similar to other regions on Mars (Irwin et al. 2013; Warner et al. 2015), the smaller area and smaller minimum diameter count reveals a significantly younger, Early Amazonian model age of 1.7 Ga when fit to $D < 1$ km. The data follow a Mars production curve over the diameter range of 200 m to 1 km along this younger isochron. This indicates that longer-term, possibly steady state modification processes that can reduce the slope of a SFD to near equilibrium are not influencing the 200 m to 1 km diameter population. Rather, the younger Early Amazonian age could suggest abrupt, yet relatively thin resurfacing of the older Hesperian-age terrain, possibly by Elysium-related volcanism. The resurfacing age and diameter range of that resurfacing (<1 km) indicates that our REC dataset, with a maximum crater size of 1.4 km, is Early Amazonian in age (1.7 Ga) and formed after resurfacing. It is therefore entirely possible that the RECs developed solely within a unit that has been developing regolith only since 1.7 Ga. Using this minimum age, a production rate of 1.8×10^{-3} mMyr⁻¹ is derived for the upper finest portion of the regolith using the 3 m thickness constraint from the Melosh (1989) excavation relationship. A rate of 1.0×10^{-2} mMyr⁻¹ is calculated accounting for a maximum 17 m thick regolith. Seventeen meters of regolith production over 1.7 Ga is a slightly higher rate than gardening models predict for Early Amazonian-age surfaces (Hartmann et al. 2001). Three meters of regolith production in that time however falls within the gardening production rate models. Higher regolith production rates here may be related to an additional input from airfall dust and wind-blown sedimentary materials that became trapped in craters.

These rates are useful for evaluating regolith thickness at the majority of Hesperian to Amazonian-age terrains where the surface processes are limited to impact gardening and eolian modification. They are, for example, consistent with the apparent vertical stratigraphy of the regolith at Hephaestus Fossae and in-situ observations at the Gusev plains by the Spirit rover (Grant et al. 2004; Golombek et al. 2016a, 2016b, this issue). However, other regions of Mars that experienced enhanced eolian, fluvial, glacial, and periglacial modification likely

exhibit a broad range of possible regolith thicknesses and the regolith thickness is likely quite variable, even for similar age terrains. As an example, the Mars Pathfinder landing site is on Hesperian age catastrophic outflow deposits that retain primary flow features that would have been destroyed by a thick regolith (Golombek et al. 1999; McEwen et al. 2005). Finally, these rates are not transferable to Noachian-age terrains when regolith production rates were significantly higher (Hartmann et al. 2001), owing to the higher impact rate.

4.3 Implications for the HP³

The HP³ is designed to measure the internal heat flow of Mars over one Mars year if it penetrates to 5 m depth (Spohn et al. 2014). It can also make this measurement by penetrating to 3 m depth, but it may take longer to fully remove the seasonal thermal wave, depending on the thermal conductivity of the regolith. For the mole to penetrate, the regolith must be loosely consolidated, contain sand to gravel-sized clasts, and lack tabular rocks or rocks whose flat face is $>45^\circ$ to the descending mole (Golombek et al. 2016b, this issue). The mole can divert around flat rocks at shallower angles; rocks >10 – 15 cm diameter with flat faces that are perpendicular to the entry angle of the probe could inhibit penetration. Mean free path calculations for volumes with surface rock abundances of $< \sim 5\%$ and established rock SFDs show a $> \sim 75\%$ probability of penetrating 3 m; lower measured rock abundances have higher probabilities (see Golombek et al. 2016b, this issue for additional probabilities for different assumptions). Our SFD comparison between NRECs and RECs from three images in the final landing ellipse (E9) suggests that 85% of that region is covered by at least a 3-m-thick regolith. While this result is derived only from a subset of three HiRISE images, the density map and subset SFD plots indicate that the three images have a distribution that is representative of the larger dataset. Our stratigraphic analysis presented in previous sections indicates that this estimate refers to the portion of the regolith that lacks meter-scale boulders. Therefore, not only is the minimum depth requirement achievable over a large area of the final landing ellipse but meter-sized clasts should be largely absent. Further, the overall lack of rocks in the exposed portions of the fine regolith in Hephaestus Fossae and its similarity in rock abundance to the adjacent cratered plains surface indicates that the regolith has a low rock abundance similar to the InSight Smooth Terrains, whose thermal inertia argues that similar properties of dominantly sand size particles extend up to 0.5 m deep (Golombek et al. 2016b, this issue). These properties indicate the Smooth Terrain will be suitable for full mole penetration (Golombek et al. 2016b, this issue).

The percent area covered by this upper column of fine regolith decreases substantially from $\sim 70\%$ at 4 m and $\sim 50\%$ at 5 m (using the Melosh 1989 excavation relationship) and thus the chance of encountering a boulder-sized clast increases as the mole approaches the desired 5 m depth. Furthermore, the density distribution of RECs suggest that specific regions of the Smooth Terrain that correspond with north-south trending wrinkle ridges may have a regolith that is locally thin relative to other areas. It is unclear how regolith development could have been influenced by the presence of a wrinkle ridge. It is possible that compression and uplift exposed rocky material throughout the time frame of regolith production. However, as the ridge appears now, there is no obvious geomorphic characteristic that might have prohibited regolith formation and preservation by impact gardening. There are very few places along the eastern ridge flank that exceed the angle of repose for cohesionless sand-sized materials ($\sim 30^\circ$). The bulk of the ridge has slopes well below this value suggesting that the slopes are stable under Mars gravity. Enhanced eolian erosion along the crest of the ridge and enhanced deposition on the sides could have thinned the regolith along the crest, relative to the sides, although we see no supporting evidence for this. Our estimated crater degradation rates do suggest that impact craters fill faster than their rims erode

in this region. Furthermore, Class 1 to Class 5 craters show a clear time series of infilling that follows a pattern of bedform migration and deposition, stabilization, and surface induration. Buried craters, filled with sand-sized materials should therefore exist within the stratigraphic column here. These predominately fine-grained crater interiors represent an ideal target for HP³ penetration.

5 Conclusion

The observed onset diameter of rocky ejecta craters at the InSight landing site in southwestern Elysium Planitia confirms the presence of a meters-thick regolith. Roll-offs in the slope of the size frequency distribution of the RECs provide a minimum measure of the regolith thickness of 2 m to 4 m, and a maximum ranging from 12 to 18 m using different excavation relationships. However, the lower constraint is more likely for the finest, boulder-free component of the regolith. The estimated regolith production rates are 1.8×10^{-3} mMyr⁻¹ to 1.0×10^{-2} mMyr⁻¹. Comparisons between the SFD of the RECs to the SFD that includes non-rocky fresh craters indicate that approximately 85% of the InSight landing area is covered with ≥ 3 m of regolith, while 50% of the area is covered with ≥ 5 m regolith. Observations of concentric craters from this region, comparisons to nearby stratigraphic exposures at Hephaestus Fossae, and regolith production models by impact gardening (Hartmann et al. 2001) are consistent with these results.

Although the relatively broad range of regolith thickness estimates could be a result of landform heterogeneities and surface processes, we conclude that a large portion of the uncertainty is due to vertical stratigraphic variations and our inclusion of any crater with ejected rocks as a rocky ejecta crater, regardless of rock abundance. We suggest that while the regolith thicknesses here are within the engineering constraints of the HP³ that the martian regolith is not uniformly fine-grained throughout the vertical column as it rests on top of bedrock. The near complete lack of ejected rocks in <30 m sized craters at the InSight landing site and the very low rock abundance in the cross section of the upper unit at Hephaestus Fossae confirms that a fine-grained regolith caps the stratigraphy of Early Amazonian to Hesperian-age plains material. However, this unit likely grades at depth into a blocky, brecciated unit that represents a coarser fraction of the regolith. The relatively lower rock abundance in the ejecta of the smaller RECs (<10% CFA) relative to the >200 m diameter RECs (<35% CFA) supports this conclusion. We therefore predict that the probability of contact with boulder-sized clasts by the HP³ will increase significantly at depths above 3 m to 5 m as the mole approaches the coarser fraction of the deeper regolith. At greater than approximately 12 m to 18 m depth but less than 200 m depth, the InSight landing region is everywhere underlain by bedrock of likely igneous origin.

Importantly, the regolith thickness estimates here account for surface processes that contributed to SFD roll-offs through the preferential obliteration of smaller craters and ejecta rocks. A similar methodology should be applied when estimating regolith thickness using the SFD of rocky ejecta craters on other martian terrains because local degradational mechanisms play an important role in masking the regolith buffering effect. At the InSight landing site, surface processes are limited to eolian modification, mass wasting, and impact gardening and our estimated crater degradation rates, rim and rock erosion rates are consistent with other Hesperian to Amazonian-age terrains that have experienced very little geologic activity (Golombek et al. 2006a, 2006b, 2014b). Our analysis is therefore most representative of regolith thickness and production rates for Hesperian to Amazonian plains units that have experienced a limited range of surface processes. The regolith estimates represent a baseline

for comparison for other plains units on Mars as well as regions that experienced additional modification.

Acknowledgements Research described in this paper was partially done by the InSight Project, Jet Propulsion Laboratory, California Institute of Technology, under a contract with the National Aeronautics and Space Administration. Warner was partially funded through the NASA Postdoctoral Program. We thank JPL interns Colin Bloom, Nate Wigton, Deborah Hernandez, Valerie Carranza, Katherine Smyth, Soumya Kannan, Caitlin Broznak, and Jeff Green with their help on this project. We also thank SUNY Geneseo student Anthony Pivarunas for his help. We are especially grateful to the Mars Reconnaissance Orbiter HiRISE (University of Arizona) and CTX (Malin Space Science Systems) imaging teams for their high-quality data and hard work in acquiring InSight imagery. We thank comments from members of the InSight science team and C. Fassett and T. Platz for constructive reviews. This paper constitutes InSight Contribution Number 24.

References

- B.W. Banerdt et al. (InSight team), InSight, a Discovery mission to explore the interior of Mars, in *44th Lunar and Planetary Science Conf.* (2013). Abstract 1915
- J.L. Banfield, Global mineral distributions on Mars. *J. Geophys. Res., Planets* (2002). doi:[10.1029/2001JE001510](https://doi.org/10.1029/2001JE001510)
- J.L. Banfield, T.D. Glotch, P.R. Christensen, Spectroscopic identification of carbonate minerals in the martian dust. *Science* **301**, 1084–1087 (2003)
- G.D. Bart, The quantitative relationship between small impact crater morphology and regolith depth. *Icarus* **235**, 130–135 (2014)
- G.D. Bart, H.J. Melosh, Using lunar boulders to distinguish primary from distant secondary impact craters. *Geophys. Res. Lett.* **34** (2007). doi:[10.1029/2007GL029306](https://doi.org/10.1029/2007GL029306)
- G.D. Bart, H.J. Melosh, Distributions of boulders ejected from lunar craters. *Icarus* **209**, 337–357 (2010)
- G.D. Bart, R.D. Nickerson, M.T. Lawder, H.J. Melosh, Global survey of lunar regolith depths from LROC images. *Icarus* **215**, 485–490 (2011)
- A.T. Basilevsky, J.W. Head, F. Horz, Survival times of meter-sized boulders on the surface of the Moon. *Planet. Space Sci.* **89**, 118–126 (2013)
- J.A. Berger et al., A global Mars dust composition refined by the alpha particle X-ray spectrometer in Gale Crater. *Geophys. Res. Lett.* **43**, 67–75 (2016)
- J.L. Bishop, S.L. Murchie, C.M. Pieters, A.P. Zent, A model for formation of dust, soil, and rock coatings on Mars; physical and chemical processes on the Martian surface. *J. Geophys. Res., Planets* **107** (2002). doi:[10.1029/2001JE001581](https://doi.org/10.1029/2001JE001581)
- C. Bloom, M. Golombek, N. Warner, N. Wigton, Size frequency distribution and ejection velocity of Corinto crater secondaries in Elysium Planitia, in *Eighth International Conference on Mars* (2014), Abstract 1289
- N. Bridges et al., Planet-wide sand motion on Mars. *Geology* **40**, 31–34 (2011)
- D.C. Catling et al., A lava sea in the northern plains of Mars: circumpolar hesperian oceans reconsidered, in *42nd Lunar and Planetary Science Conference* (2011), Abstract 2529
- D.C. Catling, C.B. Leovy, S.E. Wood, M.D. Day, Does the Vastitas Borealis formation contain oceanic or volcanic deposits? in *Third Conference on Early Mars* (2012), Abstract 7031
- P.R. Christensen, H.J. Moore, The martian surface layer, in *MARS*, ed. by H.H. Kieffer, B.M. Jakosky, C.W. Snyder, M.S. Matthews (University of Arizona Press, Tuscon, 1992), pp. 686–727
- M.J. Cintala, K.M. McBride, Block distributions on the lunar surface: a comparison between measurements obtained from surface and orbital photography. *NASA Tech. Memo.* **104804**, 41 (1995)
- I.J. Daubar, C.M. Dundas, S. Byrne, P. Geissler, G.D. Bart, A.S. McEwen, P.S. Russell, M. Chojnacki, M.P. Golombek, Changes in blast zone albedo patterns around new martian impact craters. *Icarus* **267**, 86–105 (2016)
- I.J. Daubar, A.S. McEwen, S. Byrne, M.R. Kennedy, B. Ivanov, The current martian cratering rate. *Icarus* **225**, 506–516 (2013)
- I.J. Daubar, M.P. Golombek, A.S. McEwen, L.L. Tornabene, F.J. Calef, R. Ferguson, R. Kirk, R. Beyer, Depth-diameter ratio of Corinto secondary craters, in *47th Lunar and Planetary Science Conference* (2016), Abstract 2950
- W. Fa, M.A. Wieczorek, Regolith thickness over the lunar nearside: results from Earth-based 70-cm Arecibo radar observations. *Icarus* **218**, 771–787 (2012)
- C.I. Fassett, B.J. Thomson, Crater degradation on the lunar maria: topographic diffusion and the rate of erosion on the Moon. *J. Geophys. Res., Planets* (2014). doi:[10.1002/2014JE004698](https://doi.org/10.1002/2014JE004698)

- R. Fergason, R.L. Kirk, G. Cushing, D.M. Galuzska, M.P. Golombek, T.M. Hare, E. Howington-Kraus, D.M. Kipp, B.L. Redding, Analysis of local slopes at the InSight landing site region. *Space Sci. Rev.* (2016), this issue. doi:[10.1007/s11214-016-0292-x](https://doi.org/10.1007/s11214-016-0292-x)
- M.P. Golombek et al., Overview of the Mars Pathfinder Mission; launch through landing, surface operations, data sets, and science results. *J. Geophys. Res., Planets* **104** (1999). doi:[10.1029/98JE02554](https://doi.org/10.1029/98JE02554)
- M.P. Golombek et al., Geology of the Gusev cratered plains from the Spirit rover traverse. *J. Geophys. Res., Planets* (2006a). doi:[10.1029/2005JE002503](https://doi.org/10.1029/2005JE002503)
- M.P. Golombek, J.A. Grant, L.S. Crumpler, R. Greeley, R.E. Arvidson, J.F. Bell, C.M. Weitz, R. Sullivan, P.R. Christensen, L.A. Soderblom, S.W. Squyres, Erosion rates at the Mars Exploration Rover landing sites and long-term climate change on Mars. *J. Geophys. Res., Planets* **111** (2006b). doi:[10.1029/2006JE002754](https://doi.org/10.1029/2006JE002754)
- M.P. Golombek, N.H. Warner, N. Wigton, C. Bloom, C. Schwartz, S. Kannan, D. Kipp, A. Huertas, B. Banerdt, Final four landing sites for the InSight geophysical lander, in *45th Lunar and Planetary Science Conference* (2014a), Abstract 1499
- M.P. Golombek, N.H. Warner, V. Ganti, M.P. Lamb, T.J. Parker, R.L. Fergason, R. Sullivan, Small crater modification on Meridiani Planum and implications for erosion rates and climate change on Mars. *J. Geophys. Res., Planets* **119** (2014b). doi:[10.1002/2014JE004658](https://doi.org/10.1002/2014JE004658)
- M. Golombek, C. Bloom, N. Wigton, N. Warner, Constraints on the age of Corinto crater from mapping secondaries in Elysium Planitia on Mars (expanded abstract), in *45th Lunar and Planetary Science* (2014c), Abstract 1470
- M.P. Golombek, N.H. Warner, I.J. Daubar, D. Kipp, A. Huertas et al., Surface and subsurface characteristics of western Elysium Planitia, Mars, in *47th Lunar and Planetary Science Conference* (2016a), Abstract 1572
- M. Golombek, D. Kipp, N. Warner, I.J. Daubar, R. Fergason, R. Kirk, R. Beyer, A. Huertas, S. Piqueux, N. Putzig, B.A. Campbell, G.A. Morgan, C. Charalambous, W.T. Pike, K. Gwinner, F. Calef, J. Ashley, D. Kass, M. Mischna, C. Bloom, N. Wigton, C. Schwartz, H. Gengl, L. Redmond, J. Sweeney, E. Sklyanskiy, M. Lisano, J. Benardino, S. Smrekar, B. Banerdt, Selection of the InSight landing site. *Space Sci. Rev.* 1–91 (2016b), this issue. doi:[10.1007/s11214-016-0321-9](https://doi.org/10.1007/s11214-016-0321-9)
- J.A. Grant, R. Arvidson, J.F. Bell, N.A. Cabrol, M.H. Carr, P. Christensen, L. Crumpler, D.J. Des Marais, B.L. Ehlmann, J. Farmer, M. Golombek, F.D. Grant, R. Greeley, K. Herkenhoff, R. Li, H.Y. McSween, D.W. Ming, J. Moersch, J.W. Rice, S. Ruff, L. Richter, S. Squyres, R. Sullivan, C. Weitz, Surficial deposits at Gusev Crater along Spirit Rover traverses. *Science* **305**, 807–809 (2004)
- R.A.F. Grieve, P.B. Robertson, M.R. Dence, Constraints on the formation of ring impact structures, based on terrestrial data, in *Multi-Ring Basins*, ed. by P.H. Schultz, R.B. Merrill (Pergamon Press, New York, 1981), pp. 37–57
- W.K. Hartmann, Ancient lunar mega-regolith and subsurface structure. *Icarus* **18**, 634–636 (1973)
- W.K. Hartmann, Does crater “equilibrium” occur in the Solar System? *Icarus* **60**, 56–74 (1984)
- W.K. Hartmann, Martian cratering 8: isochron refinement and the chronology of Mars. *Icarus* **174**, 294–320 (2005)
- W.K. Hartmann, G. Neukum, Cratering chronology and the evolution of Mars. *Space Sci. Rev.* **96**, 165–194 (2001)
- W.K. Hartmann, Anguita J. de la Casa, M. Berman, D.D. Ryan, E. Martian, Cratering 7: the role of impact gardening. *Icarus* **149**, 37–53 (2001)
- B. Hermalyn, P.H. Schultz, Time-resolved studies of hypervelocity vertical impacts into porous particulate targets: effects of projectile density on early-time coupling and crater growth. *Icarus* **216**, 269–279 (2011). doi:[10.1016/j.icarus.2011.09.008](https://doi.org/10.1016/j.icarus.2011.09.008)
- C.B. Hundal, M.P. Golombek, I.J. Daubar, Chronology of fresh rayed craters in Elysium Planitia, Mars: (expanded abstract), in *48th Lunar and Planetary Science* (Lunar and Planetary Institute, Houston, 2017), Abstract #1726
- R.P. Irwin, K.L. Tanaka, S.J. Robbins, Distribution of Early, Middle, and Late Noachian cratered surfaces in the Martian highlands: Implications for resurfacing events and processes. *J. Geophys. Res., Planets* **118** (2013). doi:[10.1002/jgre.20053](https://doi.org/10.1002/jgre.20053)
- B.A. Ivanov, Mars/Moon cratering rate ratio estimates. *Space Sci. Rev.* **96**, 87–104 (2001)
- J.R. Johnson, W.M. Grundy, M.T. Lemmon, Dust deposition at the Mars Pathfinder landing site: observations and modeling of visible/near-infrared spectra. *Icarus* **163**, 330–346 (2003)
- R.L. Kirk et al., Ultrahigh resolution topographic mapping of Mars with MRO HiRISE stereo images: meter-scale slopes of candidate Phoenix landing sites. *J. Geophys. Res., Planets* **113** (2008). doi:[10.1029/2007JE003000](https://doi.org/10.1029/2007JE003000)
- N. Mangold, V. Ansan, P. Masson, C. Vincendon, Estimate of aeolian dust thickness in Arabia Terra, Mars I; implications of a thick mantle (>20 m) for hydrogen detection. *Geomorphologie* **2009**(1), 23–31 (2009)

- A.S. McEwen, B.S. Preblich, E.P. Turtle, N.A. Artemieva, M.P. Golombek, M. Hurst, R.L. Kirk, D.M. Burr, P.R. Christensen, The rayed crater Zunil and interpretations of small impact craters on Mars. *Icarus* **176**, 351–381 (2005)
- A.S. McEwen et al., Mars Reconnaissance Orbiter's High Resolution Imaging Science Experiment (HiRISE). *J. Geophys. Res., Planets* **112** (2007). doi:[10.1029/2005JE002605](https://doi.org/10.1029/2005JE002605)
- D.S. McKay, R.M. Fruland, G.H. Heiken, Grain size and evolution of lunar soils, in *5th Lunar and Planetary Science Conference* (1974), pp. 887–906
- D.S. McKay, G. Heiken, A. Basu, G. Blanford, S. Simon, R. Reedy, B.M. French, J. Papike, The lunar regolith, in *The Lunar Sourcebook* (Cambridge University Press, Cambridge, 1991), pp. 285–356
- H.J. Melosh, *Impact Cratering: A Geologic Process* (Oxford University Press, London, 1989), pp. 76–85
- G.G. Michael, G. Neukum, Planetary surface dating from crater size-frequency distribution measurements: partial resurfacing events and statistical age uncertainty. *Earth Planet. Sci. Lett.* **294**, 223–229 (2010)
- H.J. Moore, Large blocks around lunar craters, in analysis of Apollo 10 photography and visual observations. *NASA Spec. Publ.* **SP-232**, 26–27 (1971)
- H.J. Moore, R.J. Pike, G.E. Ulrich, Lunar terrain and traverse data for lunar roving vehicle design study. *Prelim. U. S. Geol. Surv. Rep.* (1969)
- J.M. Moore, K.S. Edgett, Hellas Planitia, Mars; site of net dust erosion and implications for the nature of basin floor deposits. *Geophys. Res. Lett.* **20**, 1599–1602 (1993)
- K. Mueller, M.P. Golombek, Compressional structures on Mars. *Annu. Rev. Earth Planet. Sci.* **32**, 435–464 (2004)
- V.R. Oberbeck, W.L. Quaide, Estimated thickness of a fragmental surface layer of Oceanus Procellarum. *J. Geophys. Res.* **72**, 4697–4704 (1967)
- V.R. Oberbeck, W.L. Quaide, Genetic implications of lunar regolith thickness variations. *Icarus* **9**, 446–465 (1968)
- J.R. Pike, Apparent depth/apparent diameter relation for lunar craters, in *8th Lunar and Planetary Science Conf.* (1977), pp. 3427–3436
- B.S. Preblich, A.S. McEwen, D.M. Studer, Mapping rays and secondary craters from Martian crater Zunil. *J. Geophys. Res., Planets* **112** (2007). doi:[10.1029/2006JE002817](https://doi.org/10.1029/2006JE002817)
- W.L. Quaide, V.R. Oberbeck, Thickness determinations of the lunar surface layer from lunar impact craters. *J. Geophys. Res.* **73**, 5247–5270 (1968)
- D. Reiss, R.D. Lorenz, Dust devil track survey at Elysium Planitia, Mars: implications for the InSight landing sites. *Icarus* **266**, 315–330 (2016)
- S.W. Ruff, Spectral evidence for zeolite in the dust on Mars. *Icarus* **168**, 131–143 (2004)
- S.W. Ruff, P.R. Christensen, D.L. Blaney, W.H. Farrand, J.R. Johnson, J.E. Michalski, J.E. Moersch, S.P. Wright, S.W. Squyres, The rocks of Gusev Crater as viewed by the Mini-TES instrument. *J. Geophys. Res., Planets* **111** (2006). doi:[10.1029/2006JE002747](https://doi.org/10.1029/2006JE002747)
- P.H. Schultz, R.R. Anderson, Asymmetry of the Manson impact structure: evidence for impact angle and direction. *Spec. Pap., Geol. Soc. Am.* **302**, 397–417 (1996). doi:[10.1130/0-8137-2302-7.397](https://doi.org/10.1130/0-8137-2302-7.397)
- L.E. Senft, S.T. Stewart, Modeling impact cratering in layered surfaces. *J. Geophys. Res., Planets* **112** (2007). doi:[10.1029/2007JE002894](https://doi.org/10.1029/2007JE002894)
- Y.G. Shkuratov, N.V. Bondarenko, Regolith layer thickness mapping of the Moon by radar and optical data. *Icarus* **149**, 329–338 (2001)
- E.M. Shoemaker, E.C. Morris, Size-frequency distribution of fragmental debris in Surveyor program results. *NASA Spec. Publ.* **184**, 82–96 (1969)
- E.M. Shoemaker, E.C. Morris, R.M. Batson, H.E. Holt, K.B. Larson, D.R. Montgomery, J.J. Rennilson, E.A. Whitaker, Television observations from Surveyor, in *Surveyor Project Final Report, Part II* (Jet Propulsion Laboratory, Pasadena, 1968), pp. 21–136
- E.M. Shoemaker, R.M. Batson, H.E. Holt, E.C. Morris, J.J. Rennilson, E.A. Whitaker, Observations of the lunar regolith and the Earth from the television camera on Surveyor 7. *J. Geophys. Res.* **74**, 6081 (1969)
- T. Spohn, M. Grott, S. Smrekar, C. Krause, T.L. Hudson, the HP3 instrument team Measuring the Martian heat flow using the Heat Flow and Physical Properties Package (HP3), in *45th Lunar and Planetary Science Conference* (2014), Abstract 1916
- D. Stoffer, D.E. Gault, J. Wedekind, G. Polkowski, Experimental hypervelocity impact into quartz sand: distribution and shock metamorphism of ejecta. *J. Geophys. Res.* **80**, 4062–4077 (1975)
- J. Sweeney, N.H. Warner, M.P. Golombek, R. Kirk, R.L. Fergason, A. Pivarunas, Crater degradation and surface erosion rates at the InSight landing site, western Elysium Planitia, Mars, in *47th Lunar Planetary Science* (2016), Abstract 1576
- K.L. Tanaka, J.A. Skinner, J.M. Dohm, R.P. Irwin, E.J. Kolb, C.M. Fortezzo, T. Platz, G.G. Michael, T.M. Hare, Geologic Map of Mars, 1:20,000,000, USGS Scientific Investigations Map 3292 (2014)
- T.W. Thompson, W.J. Roberts, W.K. Hartmann, Blocky craters: implications about the lunar megaregolith. *Moon Planets* **21**, 319–342 (1979)

- N.H. Warner, S. Gupta, F. Calef, P. Grindrod, N. Boll, K. Goddard, Minimum effective area for high resolution crater counting of martian terrains. *Icarus* **245**, 198–240 (2015)
- N.H. Warner, M.P. Golombek, J. Sweeney, A. Pivarunas, Regolith thickness estimates from the size frequency distribution of rocky ejecta craters in southwestern Elysium Planitia, Mars, in *47th Lunar and Planetary Science Conference* (2016), Abstract 2231
- B.B. Wilcox, M.S. Robinson, P.C. Thomas, B.R. Hawkes, Constraints on the depth and variability of the lunar regolith. *Meteorit. Planet. Sci.* **40**, 695–710 (2005)
- Z. Xiao, S.C. Werner, Size-frequency distribution of crater populations in equilibrium on the Moon. *J. Geophys. Res., Planets* **120** (2015). doi:[10.1002/2015JE004860](https://doi.org/10.1002/2015JE004860)